Vilniaus universitetas
Fizikos fakultetas
Lazerinių tyrimų centras

Deividas Andriukaitis

Abliacijos Efektyvumo Tyrimas Aliuminio Oksido Keramikoje Naudojant Femtosekundinį Lazerį MHz/GHz Papliūpų Režime

MAGISTRANTŪROS STUDIJŲ BAIGIAMASIS DARBAS

Lazerinių technologijų studijų programa

Studentas	Deividas Andriukaitis
Leista ginti	2024-05-24
Darbo vadovas	dr. Valdemar Stankevič
Konsultantas	dr. Andrius Žemaitis
Centro direktorius	prof. dr. Dalia Kaškelytė

Vilnius 2024

Vilnius University
Faculty of Physics
Laser Research Center

Deividas Andriukaitis

Examining Ablation Efficiency in Alumina Ceramics Utilizing Femtosecond Laser with MHz/GHz Burst Regime

MASTERS' THESIS

Laser technology study program

Student	Deividas Andriukaitis
Allowed to defend	2024-05-24
Supervisor	PhD Valdemar Stankevič
Consultant	PhD Andrius Žemaitis
Center director	PhD Dalia Kaškelytė

Vilnius 2024

Contents

Introduction

Technical ceramics are popular dielectric materials that have become increasingly popular due to their applications across various fields, including medical, automotive, and electronics industries [1]. Among these materials, alumina (Al_2O_3), zirconia (ZrO_2), and alumina nitride (AlN) stand out. Al_2O_3, in particular, is noted for its high thermal conductivity (25 W m^{-1} K^{-1}) [2], excellent electrical insulation (10^{14}–10^{16} Ωm), robust mechanical strength (600 MPa), high dielectric strength (≈ 10 kV/mm) [3], corrosion and wear resistance, low density (< 4 g/cm^3), and operational stability at temperatures above 1000°C [4]. These properties make Al_2O_3 ceramics ideal for circuit substrates in aerospace, 5G communications, high-power semiconductors, high-power LED lighting [5], wear-resistant mechanical parts, electrical insulators [6], and heat sinks [7].

Despite its advantages, processing Al_2O_3 poses significant challenges. Conventional mechanical methods such as milling, drilling, and cutting require large cutting forces [8], leading to tool wear and potential breakage of both the tool and workpiece [3]. These techniques also require expensive tools like diamond saws, which are limited in producing linear geometries [6]. Other methods, such as electrical discharge machining (EDM), struggle with non-conductive materials [5], often resulting in poor quality like cracking and rough surfaces [1]. Similarly, mechanical punching is limited to a few hundred micrometers [2] and frequently causes substrate breakage [3]. More advanced techniques, such as electron beam processing and abrasive water jet methods, are either too expensive or lack precision [5].

Laser-based processing techniques offer a solution to these challenges. Since the invention of the ruby laser by T.H. Maiman in 1960, lasers have revolutionized material processing [9]. Lasers provide high precision, the ability to create complex geometries and patterns, non-contact processing that eliminates tool wear, and the versatility to process various materials. The creation of chirped pulse amplification led to the development of ultra-short laser pulses, ranging from tens of picoseconds to tens of femtoseconds. These ultra-fast lasers have shown significant benefits in material micromachining, reducing thermal loads and enhancing processing quality.

Early studies, for example, by S. Küper *et al.*, highlighted the advantages of ultra-short laser pulses over longer pulses. For instance, processing polymethyl-methacrylate (PMMA) with 300 fs pulses required less energy than with 16 ns pulses, significantly reducing thermal effects [**?**]. Similarly, B. N. Chichkov *et al.*, demonstrated that 250 fs pulses produced clean, sharp-edged holes in steel foil without thermal defects, unlike 3.3 ns pulses (Fig. 1) [10]. These findings showcased the potential of ultra-fast lasers in processing various materials and this holds as well for ceramics like Al_2O_3, which has been processed with ultra-short laser sources for various applications, including trimming turbine blade cores [11], drilling substrates [3, 5], and cutting Al_2O_3 substrates [6].

Ultra-short laser technology has matured and is now used in industrial applications, such as LASIK eye surgery [12], fabricating microparts, lab-on-chip devices, and welding glass [13]. The use of ultra-short laser sources in industrial applications is limited by process rate (or throughput), which is one of the significant challenges yet to overcome [6,14]. To enhance throughput, techniques such as optimizing pulse overlap, beam splitting, beam enlargement, or increasing pulse repetition

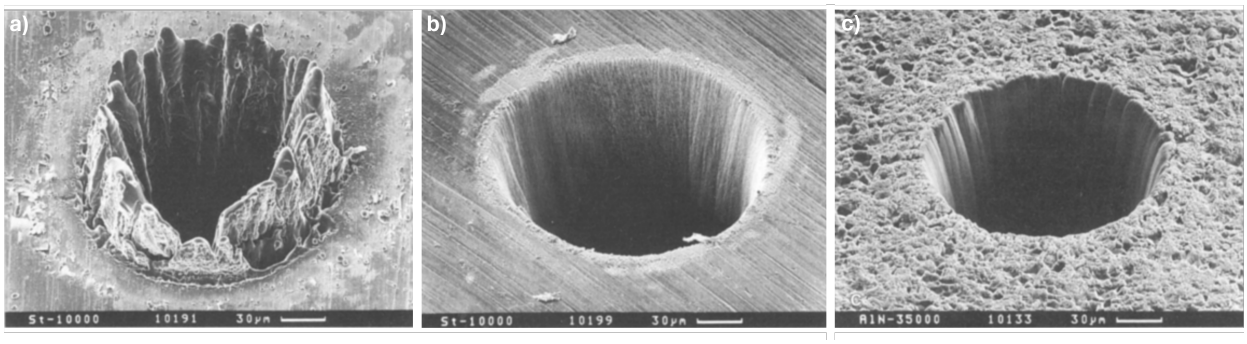

Figure 1. Scanning electron microscope (SEM) images of a) thick steel foil drilled with 3.3 ns pulses b) thick steel foil drilled with 200 fs pulses and c) AlN sample ablation with 250 fs pulses [10].

rates are used, each with pros and cons [15].

Recently, burst mode has emerged as a promising method to increase process efficiency and rate. In burst mode, lasers emit bursts of ultra-short pulses at MHz/GHz frequencies, which potentially can improve the process efficiency and rate. Despite the potential benefits, there is limited number of studies on processing Al_2O_3 with MHz/GHz burst mode, motivating this study. In this study ablation threshold fluence value, ablation efficiency and ablation rate are investigated in different operation regimes: single-pulse, MHz burst and GHz burst. The work tasks are as follows:

- Investigate single-pulse, MHz burst and GHz burst regime influence on ablation threshold;
- Investigate pulse overlap influence on ablation rate and surface roughness at single-pulse, MHz burst and GHz burst regimes;
- Investigate single-pulse, MHz burst and GHz burst regime influence on ablation rate and ablation efficiency.

1. Literature Review

1.1 Dielectric Material Interaction with Ultra-Short Laser Source

Dielectric materials are known for their large bandgaps. Typically, it is challenging to induce optical excitation in these materials using visible or invisible radiation. However, shorter wavelength radiation, such as ultraviolet (UV), can excite dielectric materials since a single photon in this range has sufficient energy to excite an electron from the valence band to the conduction band. Femtosecond lasers, with pulse durations ranging from tens femtoseconds (fs) to a few picoseconds (ps), can achieve extremely high intensities (I), often exceeding gigawatts per square centimeter (GW/cm^2), especially when tightly focused. The intensity of the laser is directly proportional to the square of the electric field ($I \propto E^2$). At low electric fields, the polarization (P) of the material is linear and can be described by the equation:

$$P(t) = \epsilon_0 \chi^{(1)} E(t), \tag{1}$$

where ϵ_0 is the free space permittivity, $\chi^{(1)}$ is the linear optical susceptibility, and t is time. However, at higher intensities, where the electric field exceeds 10^7 V/m level, the polarization response becomes nonlinear [16]:

$$P(t) = \epsilon_0 \chi^{(1)} E(t) + \epsilon_0 \chi^{(2)} E^2(t) + \epsilon_0 \chi^{(3)} E^3(t), \tag{2}$$

where $\chi^{(2)}$ is the second-order nonlinear optical susceptibility and $\chi^{(3)}$ is the third-order nonlinear optical susceptibility. Different components of the non-linear polarization (eq. 2) determine the various phenomena observed in the material, for example, $\chi^{(3)}$ is responsible for phenomena such as multi-photon ionization (MPI), tunneling ionization, and avalanche ionization (Fig. 2). The third-order susceptibility ($\chi^{(3)}$) and the nonlinear interaction of the induced high-intensity laser source and dielectric material enables the optical excitation of the material, even if the single photon energy is below the material's bandgap

1.1.1 Multi-Photon Ionization

The dielectric material excitation process schematic is shown in Fig. 4. The starting process is multi-photon ionization (MPI), which is one of the primary nonlinear effects observed during the excitation of dielectric materials by ultra-short laser pulses. This process involves the simultaneous absorption of multiple photons, which collectively provide enough energy to excite an electron from the valence band to the conduction band. Unlike traditional single-photon ionization (SPI) that occurs through real energy levels, MPI occurs *via* virtual levels (Fig. 3). In the MPI process, the first photon raises the electron to a virtual energy level. Subsequent photons then excite the electron further, eventually moving it into the conduction band. These virtual levels have very short lifetimes, typically in the range of a few femtoseconds [17]. For MPI to occur, a high-intensity laser source is necessary to ensure a sufficient photon flux, enabling the simultaneous absorption

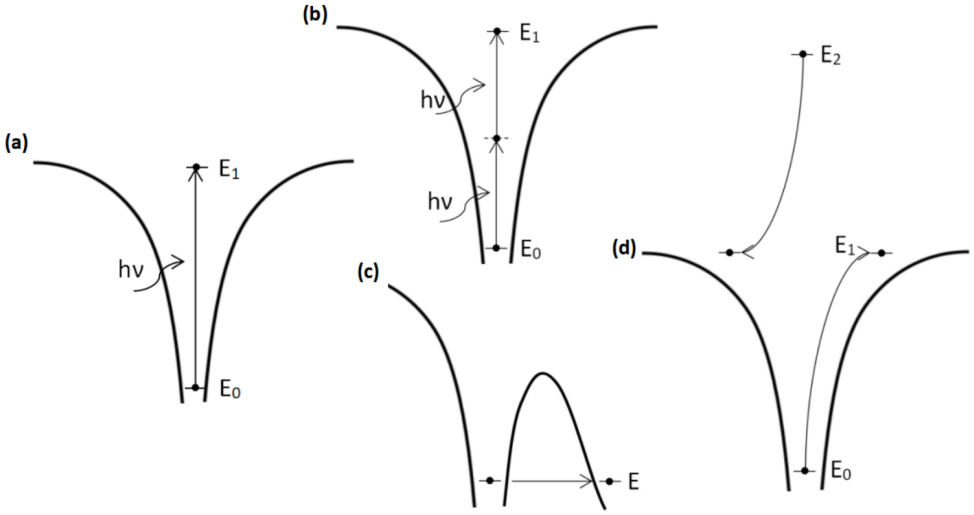

Figure 2. Schematics of nonlinear processes: (a) linear ionization, (b) multi-photon ionization (MPI), (c) tunneling ionization and (d) avalanche ionization [16]. Here hv is photon energy, E_0 is ground state of an electron, E_1 is excited state and E_2 is energy of an accelerated electron before impact to the unexcited atom.

of multiple photons.

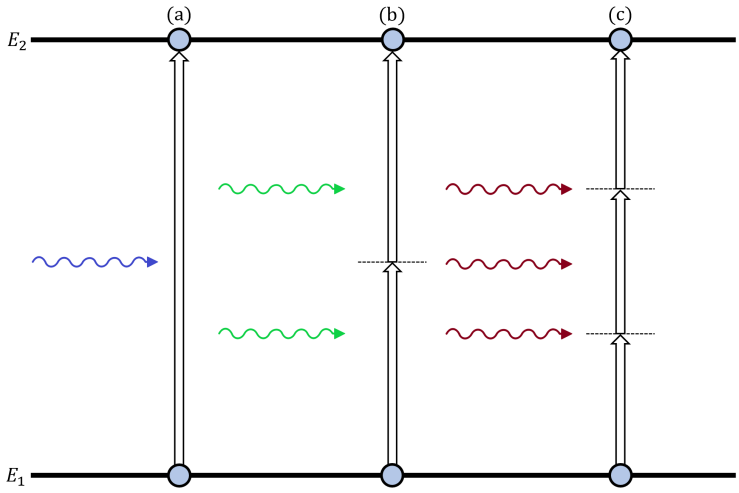

Figure 3. Schematic of one (a), two (b) and three (c) photon absorption. E_1 and E_2 indicate real energy levels, while dashed lines represent virtual energy levels.

1.1.2 Tunneling Ionization

The generation of the initial free electrons (also called "seeding" electrons) in the material usually starts with MPI, however it is worth mentioning that other nonlinear processes can generate the initial free electrons in the material. As shown in Fig. 4, another nonlinear process - tunneling ionization, also exists. This process becomes apparent when the ultra-short laser source operates at very short pulse durations, for example, $\approx$ 10 fs. At such pulse durations, the dielectric material experiences an extremely strong electric field that perturbs the Coulomb potential. Under these conditions, the electron can tunnel through the barrier, resulting in ionization. If the electric field is increased further, the potential barrier can change in such a way that ionization occurs without tunneling phenomena [19]. To better understand which nonlinear process dominates in generating the initial free electrons, one can calculate the Keldysh parameter:

$$\gamma = \frac{\omega}{\sqrt{2m^* E_g} eE}, \tag{3}$$

where ω is the electric field frequency, m^* is the effective mass of the electron, e is the electron charge, and E_g is the bandgap energy. When $\gamma \gg 1$, which is the most common case for dielectric material and ultra-short laser source interactions, the MPI process dominates. In contrary, when $\gamma \ll 1$, the tunneling ionization process becomes dominant in generating the initial free electrons in the dielectric material.

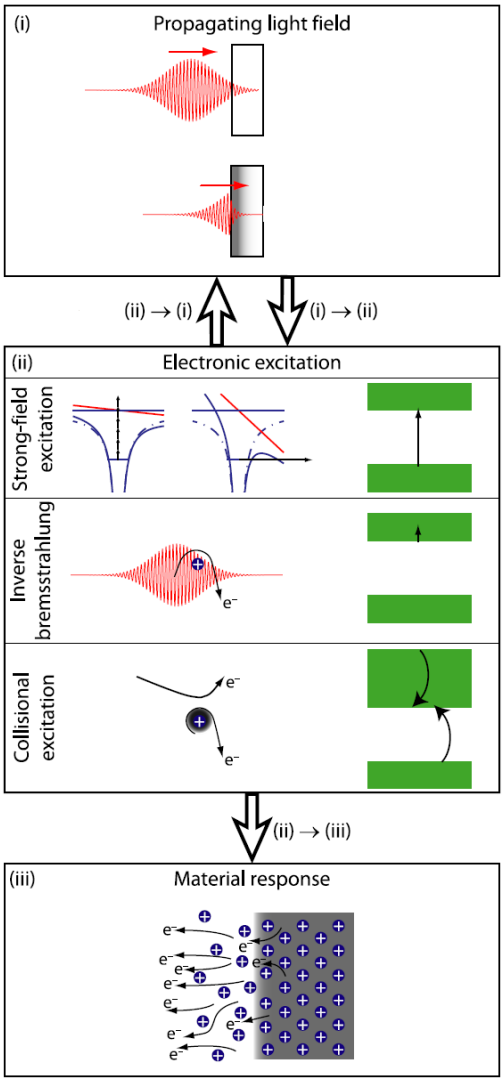

Figure 4. Schematic of excitation process of a dielectric material. (i) top figure depicts initial light interface with dielectric material, while bottom figure shows how light interacts with material in which free electron generation process is ongoing. (ii) depicts different excitation processes and (iii) shows material process once the excitation process reaches endpoint - material ejection [18].

1.1.3 Avalanche Ionization

Once a sufficient density of free electrons is generated in the dielectric material through MPI process, the material's optical properties begin to change, influencing the propagation of the induced electric field (Fig. 4 (i) bottom figure). At this stage, the free electrons behave similarly to conduction electrons in metals, which makes the dielectric material acquire metal-like properties, such as higher reflectivity and finite penetration depth. Following the MPI process, these free electrons are accelerated by the induced electric field, a phenomenon known as inverse bremsstrahlung. The elec-

trons continuously gain kinetic energy until they acquire enough energy for collisional excitation. During collisional excitation, an electron collides with an electron in valence band, promoting both electrons to the conduction band. This process, known as avalanche ionization, exponentially increases the number of free electrons. Avalanche ionization continues until a critical electron density (n_e) is reached, which can be described by the plasma frequency (ω_p) equation:

$$\omega_p = \sqrt{\frac{n_e e^2}{m_0 \epsilon_0}}, \tag{4}$$

where m_0 is the electron mass and ϵ_0 is the dielectric permeability.

Fig. 5 illustrates the evolution of electron density in response to a femtosecond laser pulse, showing the different electron generation processes and their contributions to increasing the electron density in the dielectric material. When the electron density reaches n_e, the irradiated spot becomes fully ionized, initiating the ablation process and resulting in material fragmentation.

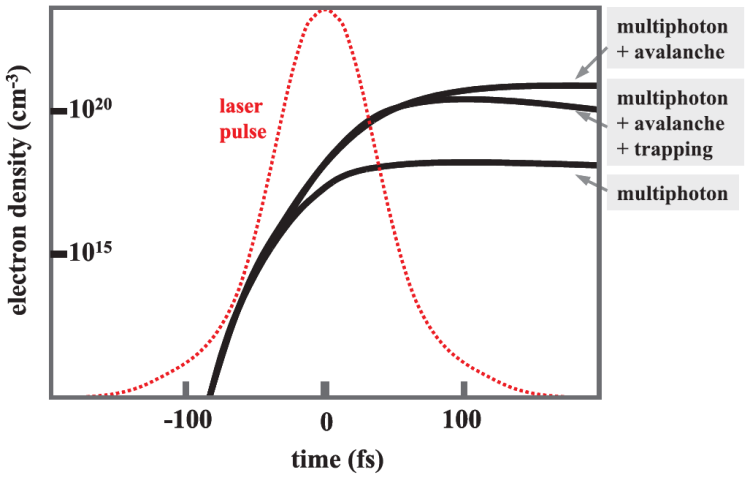

Figure 5. Schematic of electron density evolution under irradiation of 100 fs pulse. As can be seen different processes accommodate the electron density increase [19].

Material ejection during ablation can occur through two primary mechanisms: thermal and electrostatic. In thermal mechanism, the electronic system and the lattice reach thermal equilibrium, causing the material to expand. This expansion can lead to phenomena such as evaporation, plume formation, photomechanical ejection, and spallation. In electrostatic mechanism, material removal occurs due to charge separation induced by the laser's electric field. The field initiates photoemission, and due to the dielectric material's low conductivity, a local positive charge density forms (Fig. 4 (iii)). If the electrostatic repulsion force exceeds the material's binding forces, a Coulomb explosion occurs, ejecting ions [18]. The various mechanisms involved in the ablation process are depicted in Fig. 6, illustrating the different processes occurring at various timescales.

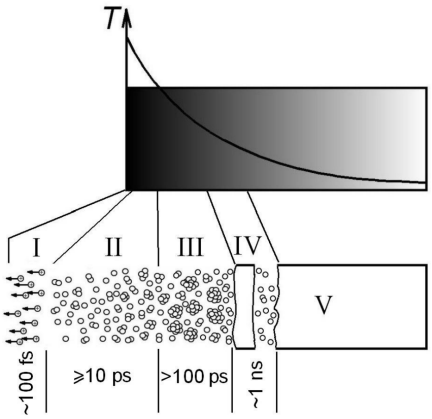

Figure 6. Schematic representation of the main ablation mechanisms under femtosecond laser irradiation. I – Coulomb explosion; II – fragmentation into plasma, atomic and small cluster state; III – phase explosion; IV – spallation [20].

1.2 Ablation Threshold and Its Measurement Techniques

When a dielectric material is irradiated by a focused femtosecond laser beam, the intensity can cause significant damage to the material. There exists a threshold fluence, known as the ablation threshold fluence (ϕ_{th}), which is necessary to reach to induce material ejection. Several methods can measure the ablation threshold, generally categorized into in-situ and ex-situ measurements. In-situ measurements do not require observable damage on the sample surface. However, they usually involve complex and expensive optical setups. Examples include time-gated imaging using backscattered light from the ablating beam [21] and interferometric techniques similar to optical coherence tomography setups [22]. On the other hand, ex-situ measurements investigates the ablated spot on the sample surface, offering a more convenient approach as they do not require complex optical setups. Often, an optical microscope is sufficient to investigate the ablated structures. However, more precise metrology setups, such as atomic force microscopy (AFM) or scanning electron microscopy (SEM), may be needed for detailed analysis [18].

1.2.1 D^2 Method for Measuring Ablation Threshold

To evaluate ϕ_{th} from the damaged spot on the sample surface, it is essential to understand the relationship between the (ϕ_{th}), the ablated spot diameter, and laser fluence. To start with, the Gaussian beam spatial fluence profile is expressed as:

$$\phi(r) = \phi_0 e^{-\frac{2r^2}{\omega_0^2}}, \tag{5}$$

where r is the distance from the beam center, ω_0 is the beam radius at the $1/e^2$ level, and ϕ_0 is the maximum laser fluence, which is expressed as:

$$\phi_0 = \frac{2E_{pulse}}{\pi\omega_0^2}. \tag{6}$$

According to Liu *et al.*, the ϕ_0 is related to ϕ_{th} and the squared ablated crater diameter (D^2) [23]:

$$D^2 = 2\omega_0^2 \ln\left(\frac{\phi_0}{\phi_{th}}\right). \tag{7}$$

This equation defines the D^2 method, in which the sample is irradiated with pulses of increasing energy. The number of incident pulses can also vary to gather more information about laser-material interactions. After irradiation, the ablated craters are inspected, and their diameters are measured together with used pulse energy.

The ϕ_0 has a linear dependence on pulse energy, which allows the determination of the ω_0 by plotting the D^2 versus the logarithm of the pulse energy. Once the graph is linearly fitted, the ω_0 is measured, and the fluence (ϕ) can be calculated and plotted in the same manner. Finally, by extrapolating D^2 to zero, one can determine the ϕ_{th} value. An exemplary plot of the D^2 method is shown in Fig. 7, where multiple datasets with different incident numbers of pulses can be plotted [24].

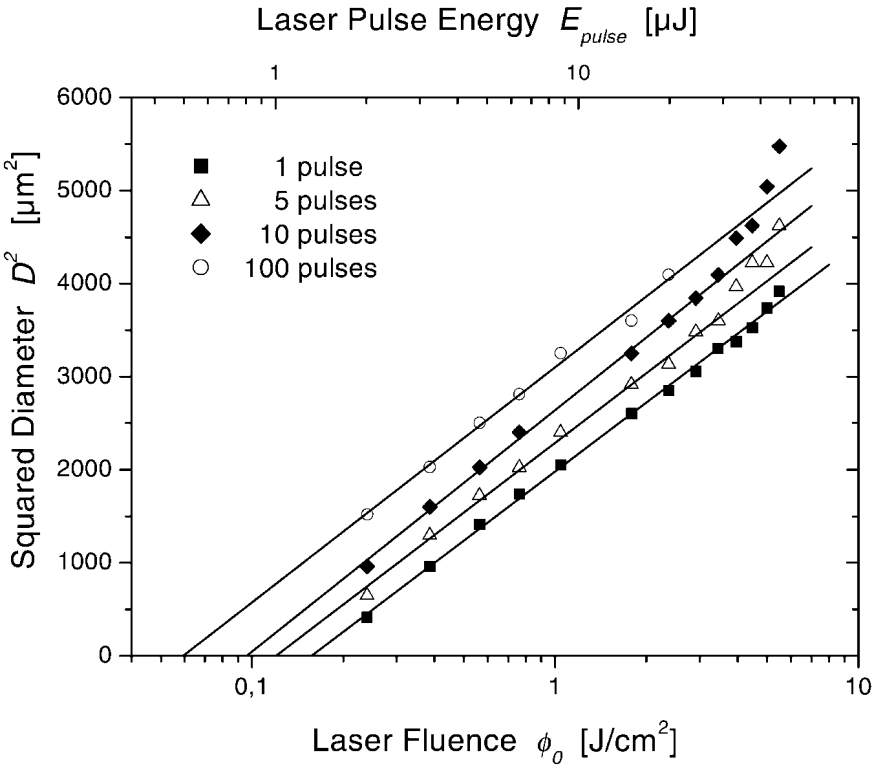

Figure 7. Squared ablated crater diameter dependence on laser fluence. Different number of pulses incident on the sample are plotted and linearly fitted to evaluate the ablation threshold fluence value [24].

Literature indicates that the ϕ_{th} value decreases with an increasing number of incident pulses on the sample. The responsible phenomenon is known as incubation [25] and has been observed in metals [26], ceramics [27], and polymers [28]. The influence of incubation on ϕ_{th} can be expressed as:

$$\phi_{th}(N) = \phi_{th}(1)N^{k-1}, \tag{8}$$

where k is the degree of incubation in the material. If $k = 1$, the ϕ_{th} is not influenced by the

number of incident pulses. The incubation phenomenon can be explained by the accumulation of defects that affect the optical properties of the material, leading to increased absorptance [29, 30].

It is also worth noting that the ablation threshold ϕ_{th} can be evaluated from the ablated crater depth. A study by L. Omenaca *et al.*, investigated laser-metal interactions by numerically solving the two-temperature model and validating the model with experiments. By varying the pulse fluence they successfully ablated craters with increasing diameters and depths. For both diameter and depth, they observed a logarithmic trend in response to the increase in fluence [31]. They used the following expression to calculate the ϕ_{th} from the ablated crater depth:

$$h = \delta \ln\left(\frac{\phi}{\phi_{th}}\right), \tag{9}$$

where h is the ablated crater depth, and δ is the optical penetration depth.

1.2.2 D-scan Method for Measuring Ablation Threshold

As an alternative to creating ablation craters to estimate the ablation threshold, the D-scan method, proposed by R. E. Samad and N. D. Vieira, can be employed [32]. This technique involves positioning the sample above the focal point and then translating it along the Y and Z axes (Fig. 8a)). This movement allows the sample to pass through the focal point, creating a "two-lobe" shape on the sample surface (Fig. 8b)). By analyzing this "two-lobe" structure, the position of the widest feature, denoted as ρ_{max}, can be measured to determine the intensity required to induce significant material modifications. The expressions for ρ_{min} and ρ_{max} representing the minimum and maximum damage radii, respectively, are given by:

$$\rho_{min} = \omega_0 \sqrt{\frac{1}{2} \ln\left(\frac{2}{\pi\omega_0^2}\frac{P_0}{I_t}\right)}, \tag{10}$$

and

$$\rho_{max} = \sqrt{\frac{1}{e\pi}\frac{P_0}{I_t}} \approx 0.342\sqrt{\frac{P_0}{I_t}}, \tag{11}$$

where P_0 is the laser power and I_t is the ablation threshold intensity, which can be expressed as:

$$I_t = \frac{P_0}{e\pi\rho_{max}^2} \approx 0.117\frac{P_0}{\rho_{max}^2}. \tag{12}$$

The D-scan method enables the determination of I_t (which, if needed, can later be recalculated to ϕ_{th}) from only two parameters: the maximum damage radius ρ_{max} and the laser power P_0.

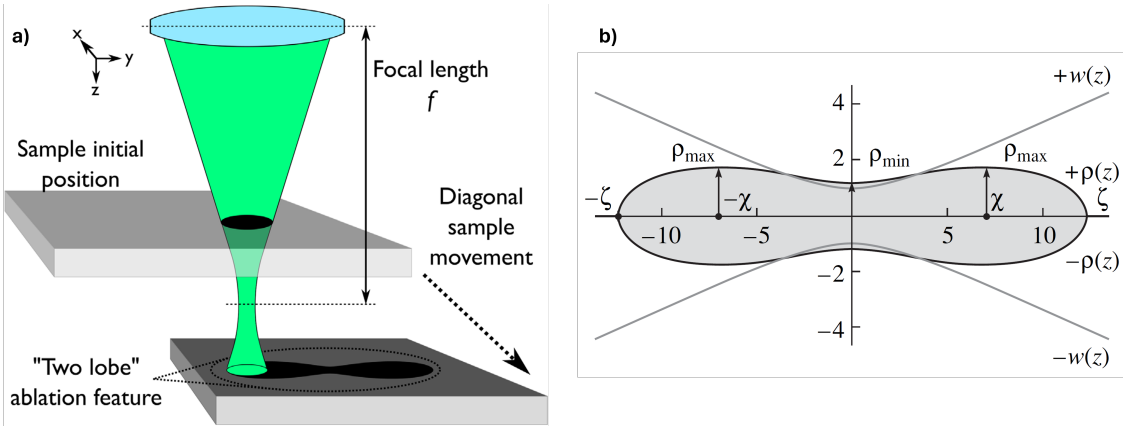

Figure 8. Schematic of the D-scan method to measure the ablation threshold. a) illustrates the technique's visual concept, with the "two-lobe" structure created by shifting the sample in the Y and Z axes [6]. b) depicts the theoretical "two-lobe" structure, indicating the minimum and maximum damage radii [32].

1.2.3 Al_2O_3 Ablation Threshold in Literature

The methods discussed above for estimating the ϕ_{th} have been applied in various studies to measure the ϕ_{th} for Al2O3. The D^2 method, for example, has been widely used in calculating the ϕ_{th}. J. Weixler *et al.*, estimated a single-shot ϕ_{th} of 0.44 J/cm^2 with an k of 0.157 and a ϕ_{th} for an infinite number of pulses of 0.14 J/cm^2 (300 fs, 515 nm) [33]. C. Kim *et al.* measured a single-shot ϕ_{th} of 2.49 J/cm^2, k of 0.92, and a ϕ_{th} for 750 incident pulses of 1.42 J/cm^2 (120 fs, 800 nm) [7]. Moreover, a study by B. Fang *et al.* used the ablated depth measurement technique to estimate ϕ_{th} and achieved ϕ_{th} values of 1.76 J/cm^2, 1.6 J/cm^2, and 1.52 J/cm^2 for the single-pulse regime, 3 pulses in the burst, and 5 pulses in the burst, respectively (burst repetition rate and number of incident pulses not specified, 400 fs, 1030 nm) [34]. R. N. Oosterbeek *et al.* used the D-scan method to estimate ϕ_{th} values of 6 J/cm^2 for single-pulse, k of 0.03, and 2.5 J/cm^2 for an infinite number of pulses (110 fs, 800 nm) [6]. It is also worth mentioning that W. Perrie observed a ϕ_{th} of 1.1 J/cm^2 by visually checking when plasma formation initiates (180 fs, 775 nm) [2], and N. Ackerl reported a ϕ_{th} value of 0.11 J/cm^2 (sub-picosecond, 515 nm) [35].

1.3 Ablation Efficiency and Ablation Rate

Femtosecond lasers, with their ultra-short pulse durations, are valuable not only for inducing non-linear processes in wide bandgap dielectric materials using visible/NIR wavelengths but also for material micromachining. One significant advantage of ultra-short pulse durations is the capability to perform "cold ablation." This phenomenon enables high-quality processing by minimizing thermal effects, which is crucial for maintaining material integrity. The key parameter facilitating cold ablation is the electron-phonon relaxation time. If the pulse duration exceeds the electron-phonon relaxation time, the excited electrons reach equilibrium with the lattice, giving rise to thermal effects such as cracks, recast layers, and surface damage (Fig. 9 (a)). On the other hand, if the pulse duration is shorter than the electron-phonon relaxation time, the energy does not transfer to the lattice, preventing significant thermal effects and ensuring higher processing quality (Fig. 9 (b)).

Despite these advantages, the integration of femtosecond lasers into industrial applications faces challenges related to process rate and efficiency. Before exploring ways to enhance the process, it is essential to understand the where the ablation efficiency and ablation rate come from.

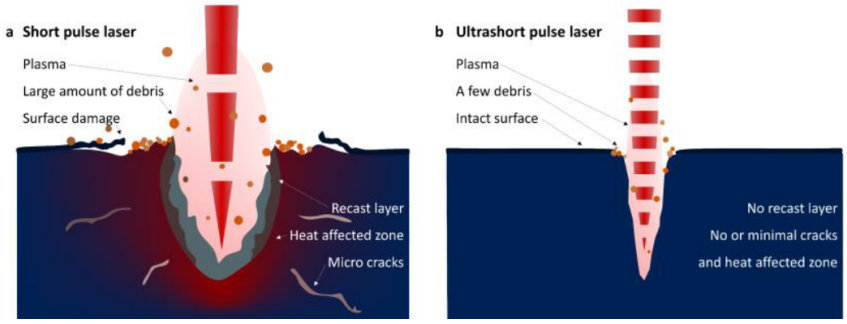

Figure 9. Schematic representation of laser-matter interaction during irradiation by (a) short laser pulses and (b) ultrashort laser pulses [15].

By using a Gaussian beam, it is possible to calculate the depth of the ablated crater [36]:

$$z(x, y) = \delta \cdot \ln\left(\frac{\phi}{\phi_{th}}\right), \tag{13}$$

where δ is the effective absorption depth. The crater diameter depends on fluence, as seen in the D^2 method. Laser fluence, related to pulse energy and beam diameter, is calculated using eq. 6. Integrating the crater profile results in the ablated volume [15]:

$$V = \frac{\pi\delta\omega_0^2}{4} \ln^2\left(\frac{\phi}{\phi_{th}}\right). \tag{14}$$

Then, the ablation efficiency can be defined as the ablated volume per unit power per time, a measure that defines how effectively the power is utilized over time (for example, mm^3/min*W):

$$\eta_E = \frac{\delta}{2\phi} \ln\left(\frac{\phi}{\phi_{th}}\right). \tag{15}$$

As for the ablation rate, it is defined by the ablated volume per unit of time (for example, mm^3/min):

$$R_t = \frac{P\delta}{2\phi} \ln^2\left(\frac{\phi}{\phi_{th}}\right), \tag{16}$$

where P is the optical power ($P = E_p f$).

It is evident, that fluence significantly influences the ablation efficiency and rate. Theoretically plotting eq. 15-16 (Fig. 10) shows that increasing fluence by raising pulse energy leads to a linear increase in ablation rate. Higher pulse energy results in more material removal. However, ablation efficiency exhibits a peak at a specific fluence, indicating the most efficient process point. This peak fluence can be calculated from eq. 15 as: $e^2\phi_{th} \approx 7.4\phi_{th}$ [36]. The most efficient ablation does not occur at maximum fluence, indicating a need to optimize laser power usage. For instance, a standard 30 W femtosecond laser system, operating at 200 kHz and focused to a 30 µm spot size, results in a fluence of 10.6 J/cm^2, much higher than the optimal fluence for processing alumina [33], giving rise to need of optimization to fully utilize the laser system's capabilities.

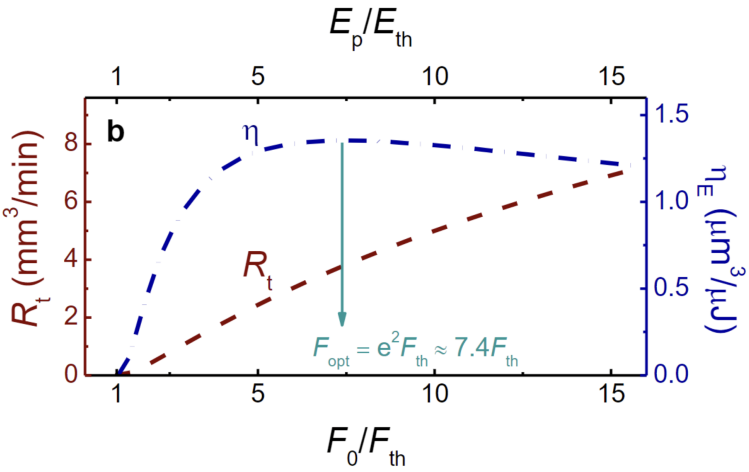

Figure 10. Theoretical plot of eq. 15-16 depicting ablation efficiency and ablation rate dependence on fluence. Conditions: δ = 50 nm and ω_0 = 20 μm [15].

1.3.1 Ablation Rate and Ablation Efficiency Optimization: Increase of Pulse Repetition Rate

One method to maintain optimal pulse fluence while utilizing the full laser power is by increasing the pulse repetition rate, which effectively reduces pulse energy and decreases pulse fluence. M. Gaidys *et al.*, demonstrated that increasing the pulse repetition rate enhances ablation efficiency and ablation rate when processing copper (Fig. 11). However, there is a limit to how much the repetition rate can be increased. Exceeding 602 kHz resulted in decreased ablation efficiency and ablation rate due to insufficient time between pulses, causing ablation particle shielding which scatters/reflects incoming pulses [37].

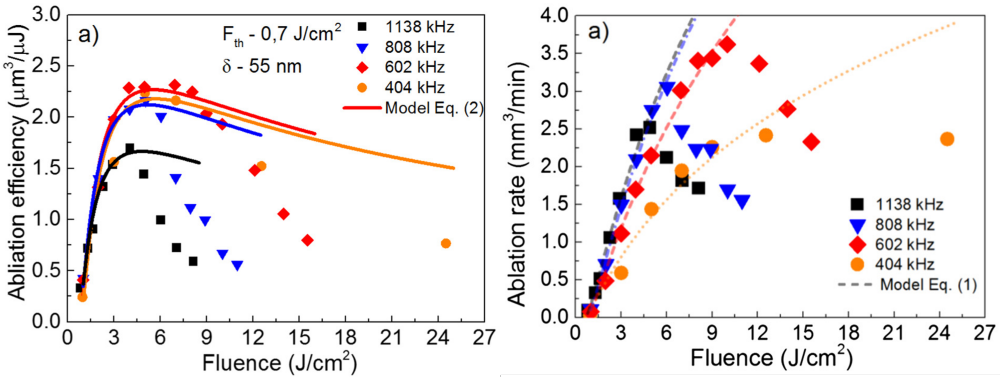

Figure 11. Ablation efficiency (left) and ablation rate (right) as functions of fluence with varying pulse energy achieved by increasing the pulse repetition rate. Increasing the pulse repetition rate reduces pulse energy, leading to higher ablation efficiency and ablation rate. However, at higher pulse repetition rates, a decrease in both ablation efficiency and ablation rate is observed due to ablation particle shielding [37].

Additionally, increasing the pulse repetition rate requires an increase in scanning speed to maintain constant pulse overlap. If not adjusted, pulse overlap percentage may increase, resulting in significant thermal effects that lead to cone-like artifacts and pores, increasing surface roughness and degrading processing quality. However, maintaining constant pulse overlap is challenging, as conventional galvanometric systems may struggle with high scanning speeds. As a solution, poly-

gon scanners can be used, which are faster, but on the other hand, are more expensive and overall complicate the processing setup [38].

1.3.2 Ablation Rate and Ablation Efficiency Optimization: Increase of Beam Diameter

Another method of decreasing the pulse fluence to an optimal value can be realized by increasing the beam diameter, which in turn decreases the pulse fluence. The eq. 13 and 15 can be depicted graphically once again, but in this case, the fluence is changed not by altering the pulse energy, but rather by adjusting the beam diameter. From the theoretical plot in Fig. 12, one can observe that ablation efficiency follows a similar trend as noticed in Fig. 10.

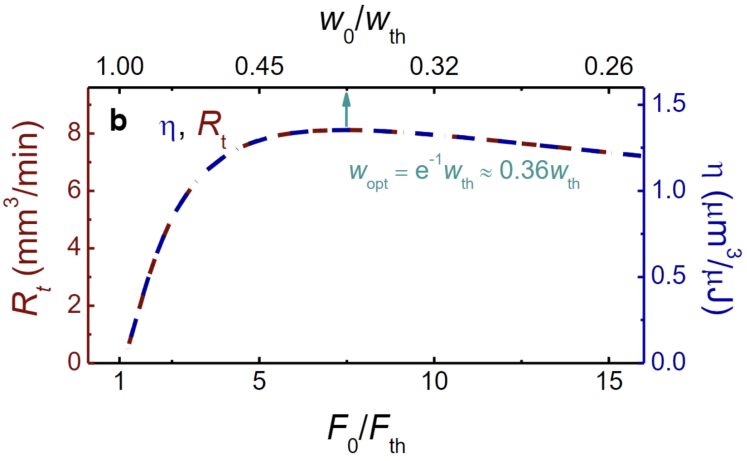

Figure 12. Theoretical plot of fluence influence on ablation efficiency and ablation rate (from eq. 14-15). Conditions: δ = 50 nm and E_{pulse} = 100 μJ [15].

However, the ablation rate dependency differs, and in this case, it has an optimal beam diameter (ω_{opt}). The optimal beam diameter can be expressed from the ϕ_{th} value:

$$\omega_{\text{opt}} = \frac{1}{e} \cdot \omega_{\text{th}} = \frac{1}{e} \cdot \sqrt{\frac{2E_p}{F_{\text{th}}\pi}}. \tag{17}$$

This theoretical estimation was tested in a study by A. Žemaitis *et al.*, where copper targets were processed with fixed optical power and pulse repetition rate. The fluence was changed by altering the sample's vertical position. As a result, the ablation rate and ablation efficiency saturated after reaching the ω_{opt} value (Fig. 13). The main advantage of this technique is that the laser can be fully utilized without complicating the processing setup. However, increasing the beam diameter may be a disadvantage for applications where a small feature size is needed [39].

1.3.3 Ablation Rate and Ablation Efficiency Optimization: Burst Mode

With ongoing development in the ultra-short laser source field, burst mode was introduced to such laser sources. Burst mode offers a unique way to reduce the pulse fluence to an optimal value, at the same time, avoiding disadvantages of other optimization methods, previously mentioned. An ultra-short laser source operating in burst mode outputs bursts composed of tightly packed ultra-short pulses with intra-burst repetition rates in the MHz and GHz range, giving rise to the names

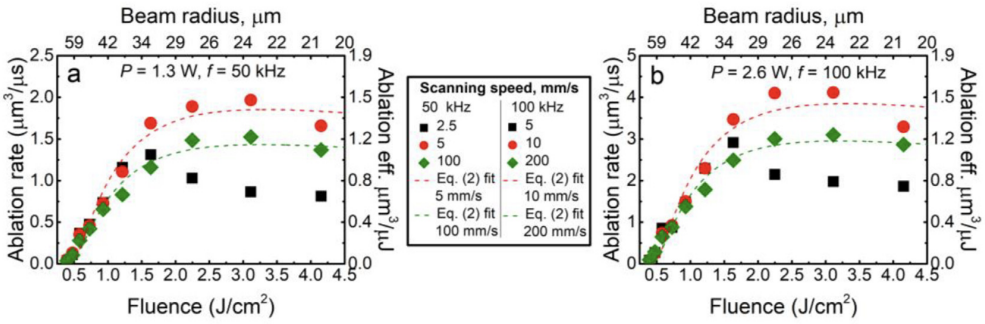

Figure 13. Ablation rate and ablation efficiency dependence on fluence, when beam diameter is altered. Different parameter sets were used: on left, P = 1.3 W, f = 50 kHz and on right, P = 2.6 W, f = 100 kHz. After reaching optimal beam diameter value, the ablation rate and ablation efficiency saturates [39].

MHz burst and GHz burst. Different ultra-short laser operation regimes are visualized in Fig. 14. The main benefit of using burst mode consists of two phenomena: decreasing the pulse fluence by dividing high-energy single pulses into multiple ones, thus reaching optimal fluence values, and laser-material interaction when the temporal distance between pulses is in the ns/ps timescale. Over time, numerous scientific articles have been published, investigating the potential benefits of burst mode in increasing not only ablation efficiency and ablation rate but also process quality.

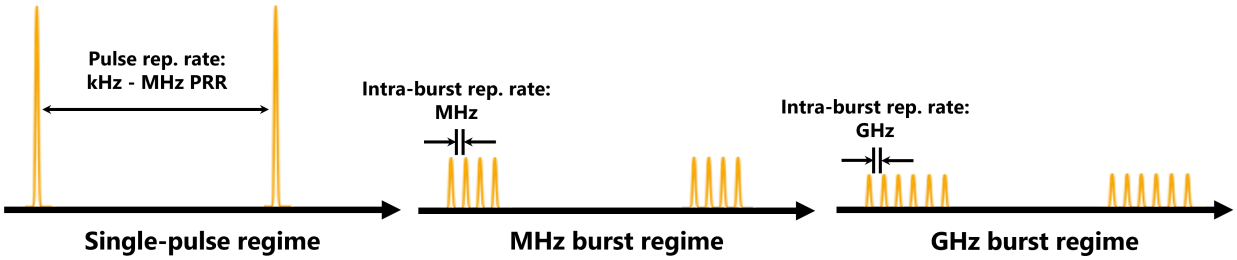

Figure 14. Schematic visualization of different operation regimes in which ultra-short pulses can operate. From left to right: single-pulse regime (pulse repetition rates from kHz to MHz), MHz burst (intra-burst repetition rate in the MHz range), and GHz burst (intra-burst repetition rate in the GHz range). Increasing the number of pulses in the burst decreases the single pulse energy within the burst accordingly.

In a detailed study by A. Žemaitis *et al.*, MHz and GHz burst modes were utilized in processing metals (64.68 MHz and 4.88 GHz burst mode, 210 fs). In MHz burst mode, processing copper resulted in a strong dependence on the odd/even number of pulses in the burst (Fig. 15. The observed ablation efficiency dependence on the odd/even number of pulses in the burst was due to shielding of the second pulse by the ablation cloud created by the first pulse. Once the third pulse arrives at the material's surface, it does not interfere with any ablation products and can interact with the material. In the case of drilling copper, 3 pulses in MHz burst resulted in 15% higher ablation efficiency than in the single-pulse regime. For cavity milling, using 3 pulses in the MHz burst resulted in 8% higher ablation efficiency than in the single-pulse regime. As for the steel samples, interestingly enough, the dependence on the odd/even number of pulses in the burst did not influence the steel sample. The highest ablation efficiency was observed for the single-pulse regime, as in steel,

MHz burst at higher fluences generated dense plasma/particles which in turn resulted in stronger shielding phenomena, resulting in lower ablation efficiencies than in the single-pulse regime. For the GHz burst mode, processing copper resulted in a 78% to approximately 90% decrease in ablation efficiency throughout the whole range of pulses in the burst compared to the single-pulse regime. Similar results were observed in steel as well; the ablation efficiency decreased from 78% to 94% compared to the single-pulse regime. The dramatic decrease in ablation efficiency in the GHz burst mode was attributed to insufficient time between two pulses, which resulted in shielding of the second pulse by generated plasma/particles from the first pulse [40].

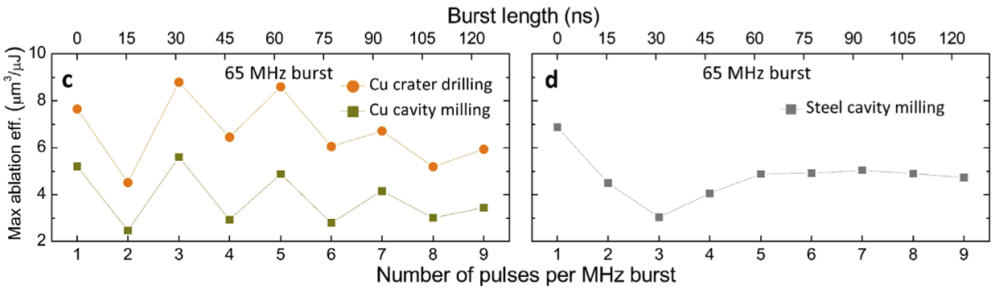

Figure 15. Maximum ablation efficiencies of drilling/milling copper plotted against the number of pulses per MHz burst, showcasing the drop in ablation efficiency for an even number of pulses in the burst due to shielding phenomena [40].

Another detailed study by N. Hodgson *et al*., investigated bursts at different intra-burst repetition rates: 60 MHz, 180 MHz, 360 MHz, 720 MHz, and 1.44 GHz. Focusing on different materials than in the previous study, at a 60 MHz intra-burst repetition rate, the authors reported an increase in ablation rate in silicon and fused silica by a factor of two when 5 or more pulses in the burst were used. Moving to higher intra-burst repetition rates, at 360 MHz and 15 pulses in the burst, the silicon ablation rate increased by a factor of 4 compared to the 60 MHz intra-burst repetition rate. The increase in ablation rate was explained as due to the interaction of intra-burst pulses on the sample. As for the 1.44 GHz intra-burst regime, no apparent increase in ablation rates was observed for steel, copper, aluminum, molybdenum, Kapton, titanium, and silicon. However, it is important to mention that at higher intra-burst repetition rates, there was no comparison with the single-pulse regime.

Taking a look at ceramics processing in the MHz/GHz burst regime, there are unfortunately very few publications. B. Fang *et al*., investigated the influence of burst mode in processing sintered alumina. The publication used a 1030 nm, 400 fs laser source which can operate in burst mode with an intra-burst repetition rate of 40 MHz. The authors reported that processing sintered alumina in MHz burst mode is beneficial in decreasing surface roughness (0.45 µm with 5 pulses in the burst, 0.5 µm in the single-pulse regime). Since the pulses in the MHz burst have lower energies, they induce gentle melting upon the sample, resulting in a higher quality surface. However, the MHz burst resulted in a drop in ablation efficiency, which was explained as the result of interaction between incoming pulses and the ablation cloud generated by previous laser pulses (Fig. 16. Due to shielding phenomena, the ablation cloud is redeposited back onto the material, resulting in lower ablation efficiencies and rates [34].

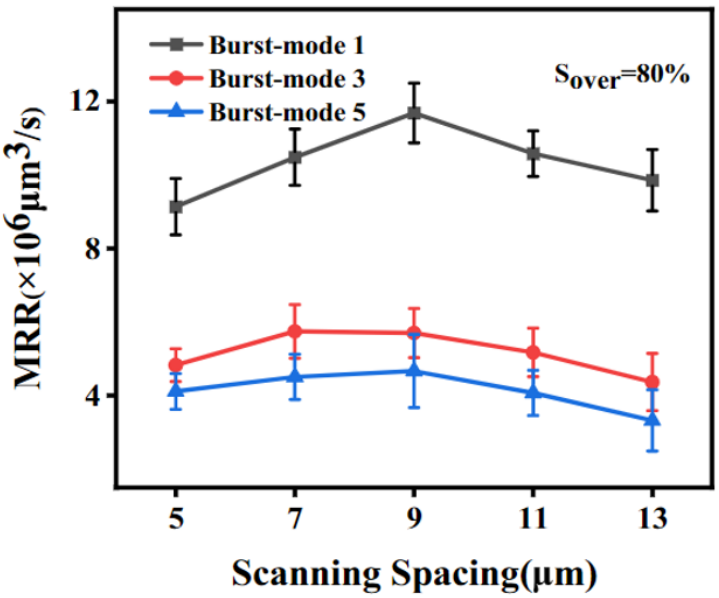

Figure 16. Ablation rate (MRR) plotted against scanning spacing for single-pulse, 3 pulses, and 5 pulses in the MHz burst regime. MHz burst results in lower MRR values, due to shielding phenomena, which redeposits ablation cloud onto the material [34].

J. Mur *et al.*, investigated the use of near-THz bursts in processing various materials, one of which was Al_2O_3. A 1064 nm laser source outputting 1.5 ps pulses was used in processing Al_2O_3 at GHz burst mode with an intra-burst rate of 440 GHz. However, increasing the pulse duration (by increasing the number of pulses) resulted in decreased ablation efficiency, which did not surpass the single-pulse regime [41]. R. Mayerhofer *et al.* used a femtosecond laser source (wavelength not specified, 700 fs) with the ability to provide a 30 MHz burst composed of 2 to 4 pulses in processing Al_2O_3 and observed a drop in ablation rate, increasing with each pulse in the burst [42]. The author did not explain the nature of the observed drop, but it might be similar to what B. Fang observed in his study - shielding phenomena induced by the first pulses and shielding the subsequent pulses.

2. Methodology

2.1 Experimental Setup

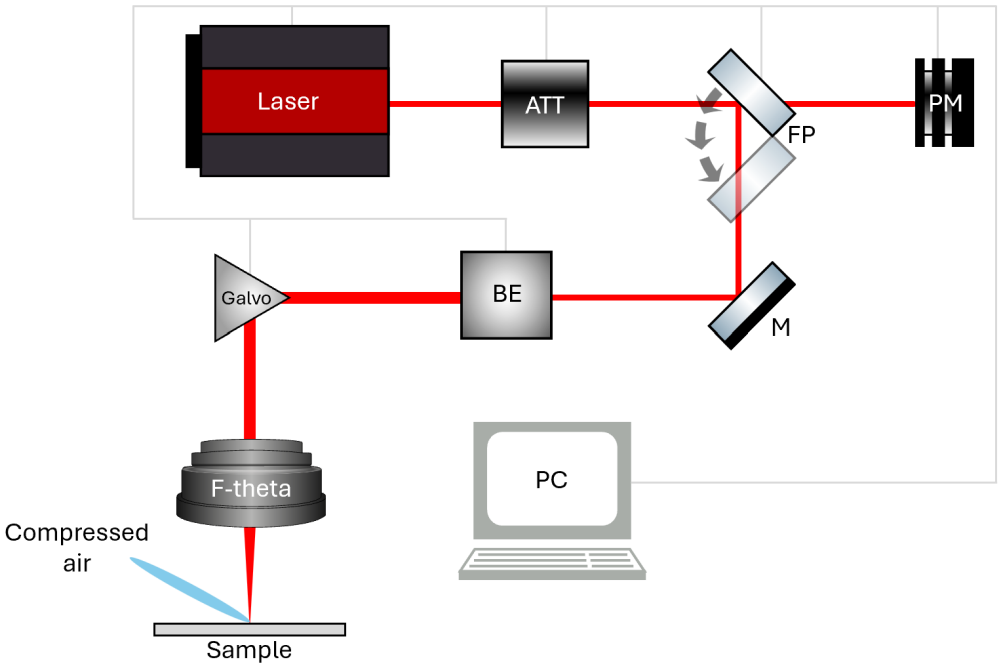

Figure 17. Laser workstation principle scheme. Laser - femtosecond laser, ATT - attenuator, FP - flip mirror, PM - powermeter, M - mirror, BE - beam expander, Galvo - galvanoemetric scanners, F-theta - focusing objective.

An open-enclosure type laser workstation (Akoneer, Lithuania), equipped with a femtosecond laser (Ekspla, Lithuania) source, was used in this work. The laser workstation's simplified principle scheme can be seen in Fig. 17. In this study, industrial grade femtosecond laser source FemtoLux 30 was used - a 30 W average power system outputting 1030 nm wavelength radiation with a tunable pulse repetition rate (200 kHz – 4 MHz) and pulse duration (350 fs – 1 ps). ATT (Akoneer, Lithuania) – attenuator for controlling the laser's output power. FP (Akoneer, Lithuania) - flip mirror, to direct the laser beam to the focusing objective or to the powermeter. PM (Gentec-EO, Canada) - powermeter to measure the laser's output power, as well as measure the calibration curve of output power versus attenuator transmission. M - mirror, to shape the laser beam's path around the laser workstation. BE - beam expander, to expand the laser beam diameter. Galvo (Scanlab, Germany) - galvanometric scanners to deflect the incident laser beam onto the sample, F-theta - F-theta lens (f=160 mm, Excelitas, USA), to focus the incoming laser beam onto the sample. Components (which are actively switched) were connected to a PC and controlled with software DMC (Direct Machining Control, Lithuania) to specify process parameters (scanning speed/geometry, attenuator's transmission, hatching/slicing steps, and many more).

The FemtoLux 30 laser source offers two different burst mode regimes. The first one is MHz burst mode, which operates at a 50 MHz intra-burst repetition rate with the possibility to change the number of pulses inside the burst from 2 to 10. The MHz burst also has an exponentially dropping

shape, which can be seen in Fig. 18 a). The second is the GHz burst mode, in which bursts of 2 GHz intra-burst repetition rate are created with the ability to change the number of pulses in the burst from 2 to 21 and from 43 to 1100. The GHz burst shape in the range from 2 to 21 pulses in the burst is square (Fig. 18 b)), while for the other range, it has an exponential decaying shape (Fig. 18 c)). It is important to mention that the burst shape is not taken into account during calculations, and it is presumed that each pulse in the burst has equal energy throughout the burst.

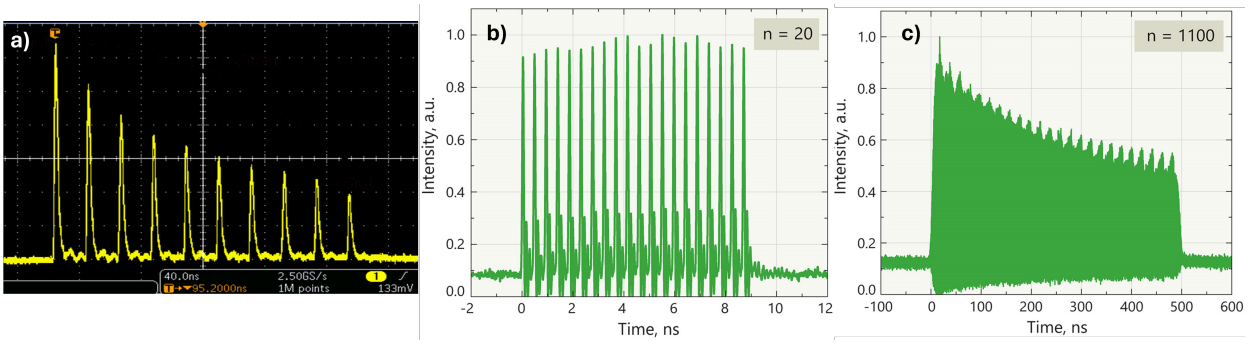

Figure 18. FemtoLux 30 operation regimes: a) MHz burst mode, 50 MHz intra-burst repetition rate, 10 pulses in the burst; GHz burst mode, 2 GHz intra-burst repetition rate, b) 20 pulses in the burst and c) 1100 pulses in the burst.

The majority of measurements of processed Al_2O_3 were taken with an optical 3D surface profiler SensoFar and afterwards analyzed with the specialized program SensoView. For smaller features, the samples were inspected with a Thermo Fischer Scientific scanning electron microscope (SEM).

3. Results and discussion

3.1 D^2 Method in Measuring Al_2O_3 Ablation Threshold

The ablation thresholds of Al_2O_3 were determined using the D^2 method, previously described in section 1.2.1. The laser operated at a pulse repetition rate of 203.2 kHz, in order to have highest energy per pulse, with a fixed pulse duration of 350 fs. Various parameters were adjusted to evaluate their impact on the ablation threshold: laser power was changed from 30% to 75%, with incremental increases of 5%; different number of incident pulses/bursts was tested (100, 500 and 1000); different operational regimes were examined, including single-pulse, MHz burst (2, 3, 5, 6, 9, and 10 pulses in the burst) and GHz burst (2, 3, 9, 10, 15, and 16 pulses in burst) regimes. In total, 43 different parameter sets were investigated to investigate ϕ_{th} and determine burst mode influence to it.

The methodology for creating craters, used to measure the ϕ_{th} is shown in Fig. 19. To increase the accuracy of the experiment, each laser power value was replicated three times. This step was required given the rough surface texture of Al_2O_3, which posed challenges in precisely measuring the diameters of the ablated craters. Hence, in total 1410 craters were formed on Al_2O_3 surface and afterwards measured by using SEM.

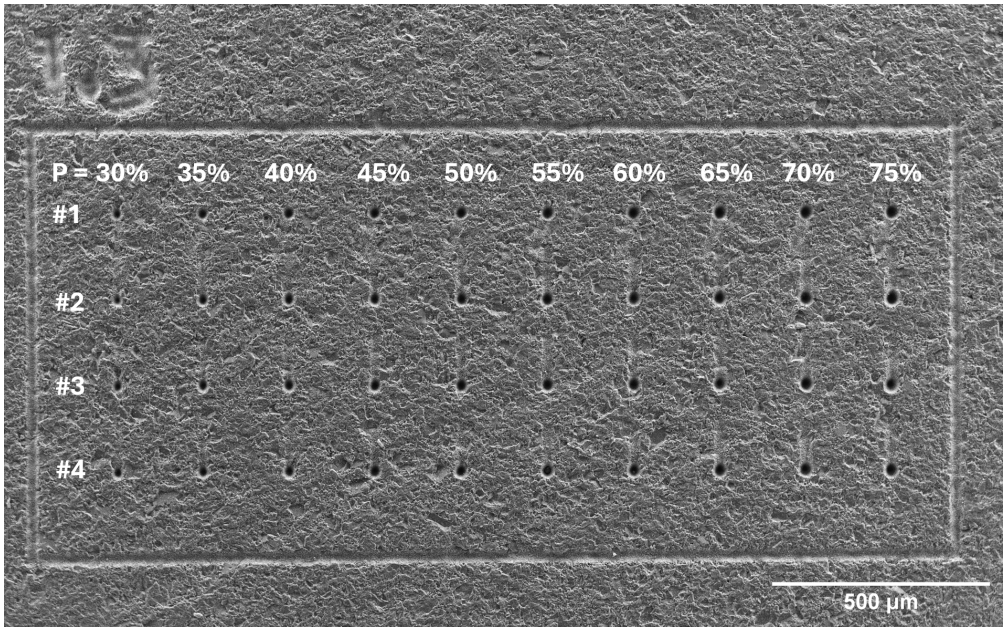

Figure 19. SEM image of one of the configurations showcasing the crater formation methodology. Each configuration was investigated by varying the laser power from 30% to 75% in 5% increments. Due to the rough surface texture and the challenge of accurately measuring the ablated crater diameter, an additional 3 craters were made for each power level.

After completing the experimental procedures, the samples were examined using SEM and each crater's diameter was measured and recorded in datasheet along with used laser power and operation regime. The beam diameter was evaluated by plotting the squared diameters of the ablated craters against the pulse energy. This data was then linearly fitted to determine the beam diameter for each configuration. The results indicated a mean beam diameter of approximately 30 µm, with a fluctuation of ± 4 µm across the different settings.

Looking in literature, various terms are used to define: fluence, laser fluence, burst fluence and pulse fluence. In this study, the pulse fluence was chosen to be used. It is expressed as:

$$\phi = \frac{2P}{\pi\omega_0^2 f n_b}, \tag{18}$$

where P - average optical power, measured by powermeter for every burst configuration, f - laser pulse repetition rate and n_b - the number of pulses in the burst. In the context of pulse fluence, it is important to take into account the number of pulses in the burst as this decreases the single pulse fluence in the burst.

After investigating the samples with SEM, the ablated crater D^2 values were graphically depicted against the pulse fluence, as illustrated in Fig. 20.

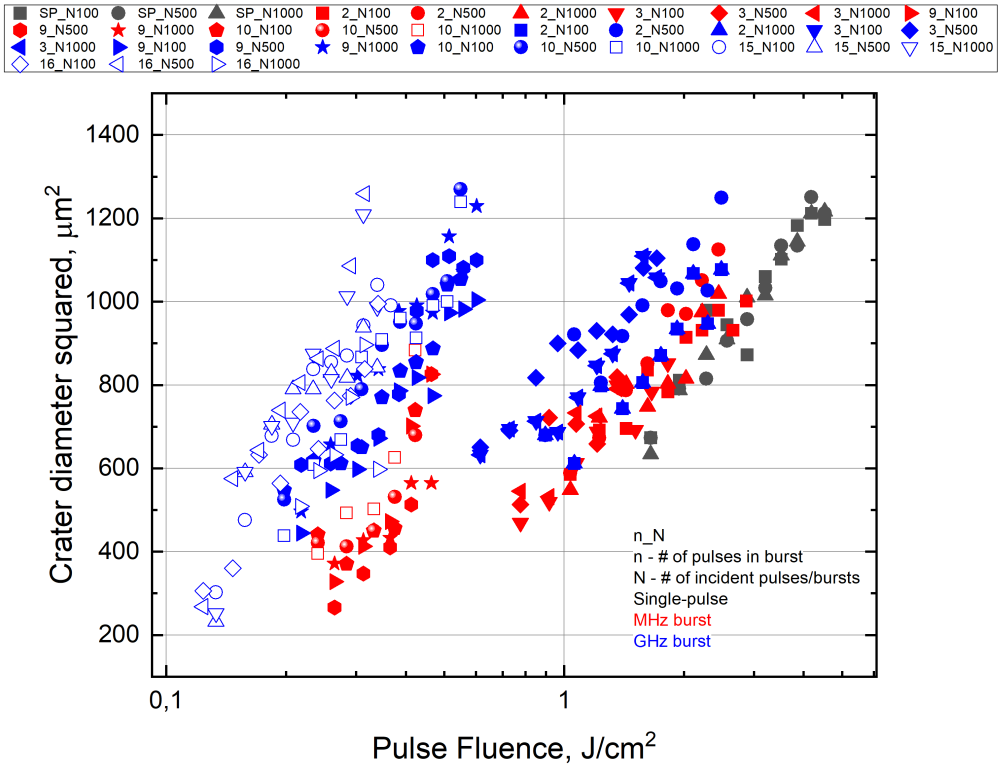

Figure 20. Squared crater diameter plotted against pulse fluence for single-pulse, MHz burst, and GHz burst regimes. The graph represents different configurations with varying numbers of pulses in the burst (2, 3, 9, 10, 15, 16) and different numbers of incident pulses/bursts (100, 500, 1000). Color indication: black - single-pulse regime, red - MHz burst regime and blue - GHz burst regime. The graph shows that as the pulse fluence increases, the crater diameter increases across all configurations.

The graph demonstrates a consistent trend across all configurations: as the pulse fluence increases, so does the crater diameter. However, none of the configurations resulted in a substantial increase in crater size. Interestingly, even when pulse fluence is reduced significantly in burst mode (16 pulses in GHz burst lowers pulse fluence from approximately 1.65 to 0.13 J/cm^2), ablated craters remain visible and measurable.

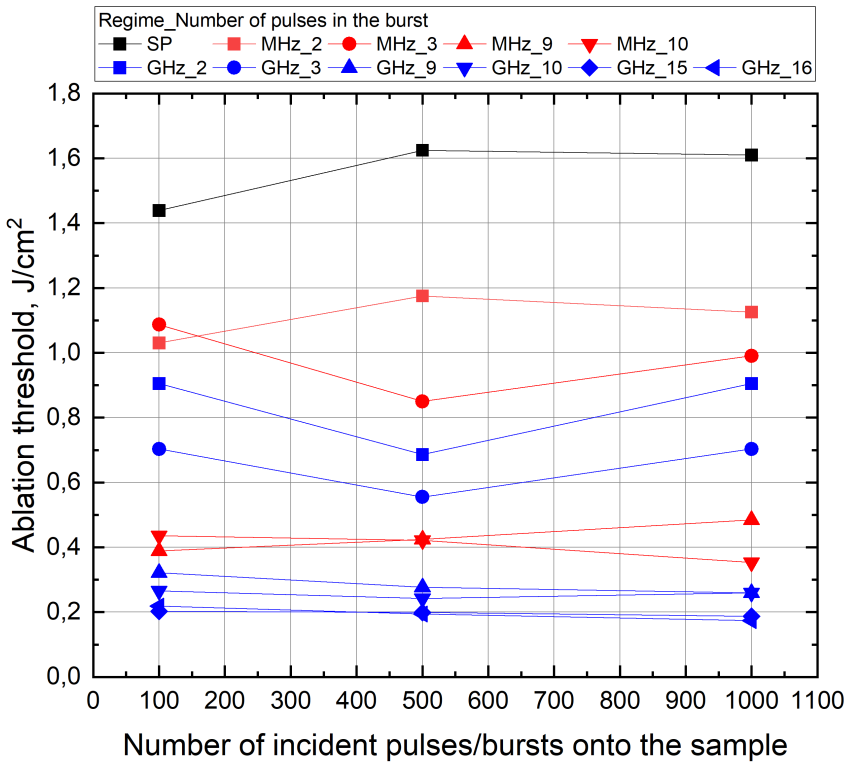

Figure 21. Measured ablation thresholds for various configurations plotted against the number of incident pulses/bursts. The graph illustrates how the ablation threshold changes as the number of pulses in the burst increases for both MHz and GHz burst regimes, as well as the total number of incident pulses/bursts on the sample.

Moving on, the ϕ_{th} values for various configurations were calculated by using linear fit function on the curves shown in Fig. 20. Calculated ϕ_{th} values were then plotted against the number of incident pulses/bursts on the sample in Fig. 21. A noticeable trend is that increasing the number of pulses in a burst decreases the ϕ_{th} value, which can be seen in Fig. 22 which shows Fig. 21 slice at number of incident pulses/bursts onto sample of 1000. This trend was expected, as increasing the number of pulses in the burst, decreases the single pulse energy, simultaneously decreasing the pulse fluence as well. In addition, as it can be seen in Fig. 20, at very low pulse fluences (for ex. GHz burst with 16 pulses) the ablated crater diameter is still observable, which essentially results in lower ϕ_{th} values with increase in number of pulses in the burst.

Looking back at Fig. 21 it was observed that, for example, using 3 pulses in both MHz and GHz bursts results in lower ϕ_{th} values for GHz burst regime compared to MHz burst regime. There are two reasons for such observation. From one side, as previously discussed, the pulses in MHz burst suffers from shielding effect, which is induced from the first pulses interacting with the material and producing an ablation cloud that shields other pulses [34]. From another side, in GHz burst, due to short temporal distance between adjacent pulses in the burst, each pulse contributes to the ablation mechanism, increasing the efficiency of the process and further decreasing the ϕ_{th} value [43].

The lowest ϕ_{th} value was observed for GHz burst regime with 16 pulses in the burst, resulting in 0.2 J/cm^2. This was achieved by splitting the high energy pulse into multiple ones, essentially decreasing single pulse fluence in the burst down to $\approx$ 0.12 J/cm^2. The crater formation on sample

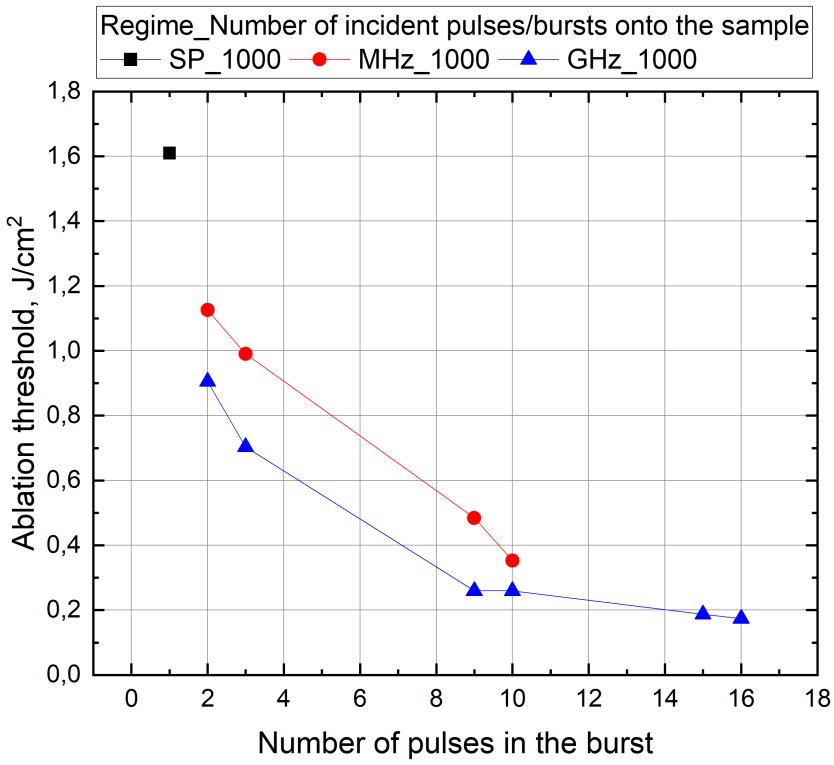

Figure 22. Measured ablation thresholds at a fixed number of incident pulses/bursts (1000), plotted against the number of pulses in the burst. The graph shows that increasing the number of pulses in the burst leads to a decrease in the ablation threshold. This decrease is due to the lower pulse fluence in burst mode, which still manages to ablate the material.

surface at single pulse fluences lower than ϕ_{th} was possible thanks to high intra-burst repetition rate of GHz burst. First pulses in the burst heat the material, which ϕ_{th} value decreases with increase in temperature. Once the material is heated enough, single pulse fluence is sufficient to initiate the ablation process, which leads to efficient material removal at low fluence levels. Hence, even though the measured ϕ_{th} is higher than single pulse fluence in the burst, due to GHz burst regime, ablation at pulse fluences below ϕ_{th} are possible [43].

Scientific articles, as mentioned in section 1.2.3, generally start ablation threshold experiments with a lower number of pulses/bursts incident on the sample (1, 5, 10, etc.). For this experiment, however, the number of incident pulses was set at 100, since tests with 1, 5, 10, and 50 pulses did not result in significant damage that could be easily distinguished, especially considering the challenge posed by the naturally rough surface of the material in identifying the ablated craters. In addition, as can be seen in Fig. 21 the ϕ_{th} value does not decrease with increase in number of incident pulses/bursts onto the sample, which contradicts with findings from literature regarding the incubation factor mentioned earlier in section 1.2.1. The increase in number of incident pulses/bursts onto the sample results in saturation of ablation threshold (with some deviation due to accuracy of measuring the ablated crater diameters), which has been observed also in investigating the ablation threshold of quartz in a study by R. de Palo *et al*. The publication showcases that the ϕ_{th} value decreases until the incident number of pulses reach value of 100, after it, the ablation threshold saturates (Fig. 23). The saturation phenomena was explained as creation of defect sites

in the material, such as color centers and Frenkel pairs, which are formed when the generated free electrons eventually relax in the material [29]. These defects then can generate additional energy levels in the material which act as additional excitation routes for the free electrons. This saturation phenomena could be called metallization, because eventually due to these defects, the dielectric bandgap will be filled with energy states from the defects and in result the electronic system will be metal-like [44]. So, in order to have lower incident number of pulses/burst incident onto the sample, one should look into polishing the sample, so the ablated crater would stand out or look into other ablation threshold measurement methods such as D-scan.

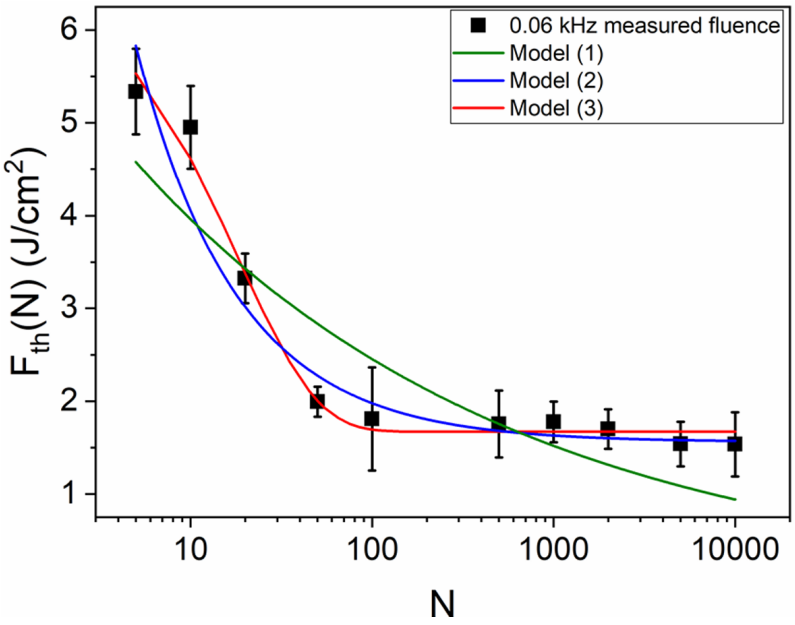

Figure 23. Ablation threshold measurement of quartz. The graph depicts multi-pulse ablation threshold fluence against the number of incident pulses [44].

Moreover, as mentioned in the methodology section, the laser source is capable of delivering a higher number of pulses in GHz burst mode than was tested. The limitation arises because, with a larger number of pulses per burst, significant thermal effects become evident in the material. These effects distort the shape of the craters, resulting in non-circular forms and melted material around the crater, which complicates the accurate measurement of crater diameters. This phenomenon is illustrated in Fig. 24. Due to this limitation, up to 16 pulses per burst were measured accurately with the D^2 method. In order to measure the ablation threshold value for larger number of pulses in the burst, one can look at alternative methods such has D-scan or ablation threshold measurement from measuring the ablated structure depth.

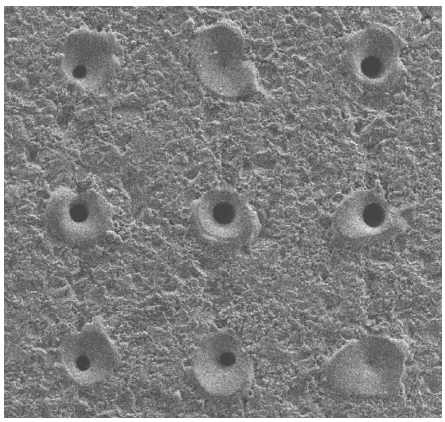

Figure 24. SEM image of ablation threshold measurement at 43 pulses in GHz burst with 100 incident bursts on the sample. Such irradiation configuration results in severe melting which makes the ablated crater diameter immeasurable due to melted material around the ablated crater.

Table 1. Ablation threshold values with corresponding laser source parameters.

Ablation threshold value (J/cm^2)	**Laser source used**	**Citation number**
0.44	300 fs, 515 nm	[33]
2.49	120 fs, 800 nm	[7]
1.76	400 fs, 1030 nm	[34]
1.6 (burst mode, 3 pulses)	400 fs, 1030 nm	[34]
1.52 (burst mode, 5 pulses)	400 fs, 1030 nm	[34]
6	110 fs, 800 nm	
1.1	180 fs, 775 nm	[2]
0.11	sub-picosecond, 515 nm	[35]
1.44, single-pulse, N=100	350 fs, 1030 nm	this study
1.09, MHz burst, 3 pulses, N=100	350 fs, 1030 nm	this study
0.39, MHz burst, 9 pulses, N=100	350 fs, 1030 nm	this study
0.7, GHz burst, 3 pulses, N=100	350 fs, 1030 nm	this study
0.26, GHz burst, 9 pulses, N=100	350 fs, 1030 nm	this study
0.2, GHz burst, 16 pulses, N=100	350 fs, 1030 nm	this study

In Table 1, the ϕ_{th} from the literature are compared with those calculated in this study. The table shows that the ϕ_{th} are quite scattered. The value measured in this study for the single-pulse regime is somewhat similar to those reported by N. Ackerl *et al*. [35] and W. Perrie *et al*. [2]. The differences in ablation threshold values could be attributed to variations in wavelengths [45], sample surface roughness [46], and pulse durations [47]. Variations in wavelength affect the absorption efficiency of the laser energy by the material, with shorter wavelengths generally providing higher energy photons that can more effectively induce ablation [45]. Sample surface roughness can influence the energy distribution, where rough surfaces can cause scattering and non-uniform energy deposition [46]. Pulse duration influences the interaction time between the laser and the material. Shorter pulses reduce thermal diffusion into the material, leading to more efficient ablation [47]. Additionally, it is worth noting that, as observed in the study by B. Fang *et al.* [34], the ϕ_{th} value decreases with an increase in the number of pulses in the burst, which was observed in this study, most probably due to reduction of single pulse fluence in MHz burst and ablation of crater with di-

ameter similar to configurations with lower number of pulses in MHz burst, which results in lower ϕ_{th} values.

3.2 Investigation of Ablation Efficiency and Ablation Rate

To investigate the influence of burst mode on ablation efficiency and ablation rate, 1x1 mm^2 squares were milled on the Al_2O_3 sample surface, and their depths were subsequently measured. The ablation process involved various fabrication parameters: pulse overlap, number of scanned layers, laser power, and scanning angle. Laser power was adjusted using an external attenuator (Fig. 17 ATT), and the number of scanned layers was kept at 5. This number of layers ensured that the ablated depth was sufficient to be measured by the 3D surface profiler. The focus position was maintained at the sample surface and was not adjusted throughout the milling process.

During the initial experiments, the scanning angle was set to rotate by 90 degrees with each scanning layer. However, during the measurement stage with the optical profilometer, scanning artifacts (grid-like structures) were observed on the surface of the ablated square, as depicted in Fig. 25. Similar surface structures have been reported in other studies. G. Mincuzzi *et al*. stated that scanning angles that are not multiples of 30 degrees help ensure an even distribution of laser pulses on the material [48]. Additionally, C. Li *et al*. noted that non-regular scanning angles prevent the formation of repetitive patterns that lead to grid-like structures, as observed in this study, and also contribute to achieving a smoother surface finish [49]. To avoid these scanning artifacts, scanning angle of 11 degrees was chosen.

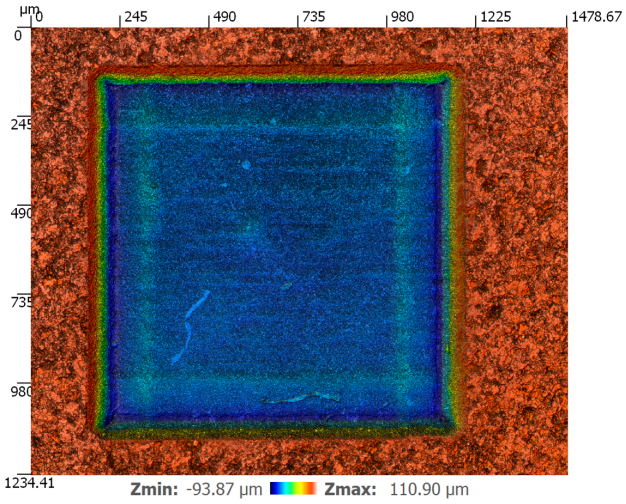

Figure 25. 3D optical profilometer image of an ablated square with a scanning angle rotation of 90 degrees, resulting in a grid-like structure on the ablated surface due to formation of repetitive patterns.

3.2.1 Pulse Overlap Influence on Ablation Rate and Surface Roughness in Different Operation Regimes

Before investigating the influence of burst mode, the effect of pulse overlap in milling squares was examined to optimize the process. The pulse overlap depicts the percentage by which laser

pulses overlap on the material's surface and can be expressed as:

$$PO = \frac{2\omega_0 - x}{2\omega_0} \times 100\%, \quad x = \frac{v}{f}, \tag{19}$$

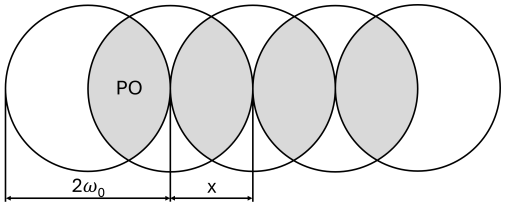

Figure 26. Schematic visualization of the pulse overlap.

where v is the scanning speed (mm/s). It is important to mention that the pulse overlap in this study is identical in X and Y directions, because in some studies, hatching term is used, which depicts the irradiated line overlap with another line. Beam spot diameter was calculated from ϕ_{th} measurement, which is equal to 30 µm. Various pulse overlap values were chosen for investigation: 50%, 60%, 70%, 80%, 90%, 93%, and 95%. These pulse overlap values were tested in different operation regimes: single-pulse, MHz burst (with 2, 3, 5, 6, 9, and 10 pulses per burst), and GHz burst (with 2, 3, 5, 6, 9, 10, 15, 16, 20, 21, 43, 44, 64, and 65 pulses per burst). To simplify the experiment, 50% of the laser power was used. In total, 147 squares were milled with different processing parameters. After laser processing, the sample was examined with a 3D optical profilometer, and the depths of the ablated squares were measured (Fig. 27). In Fig. 27 the profiles of the ablated squares show that at high pulse overlap values (93% and 95%), the material experiences overheating, leading to material redeposition, eventually reducing the ablated volume. However, in the MHz burst mode, the overheating effect was less pronounced, resulting in more volume being ablated, although not entirely avoided. In the GHz burst mode, by splitting the high-energy pulse into multiple pulses (in this case 43 pulses), the material did not experience overheating, resulting in a cleanly ablated square.

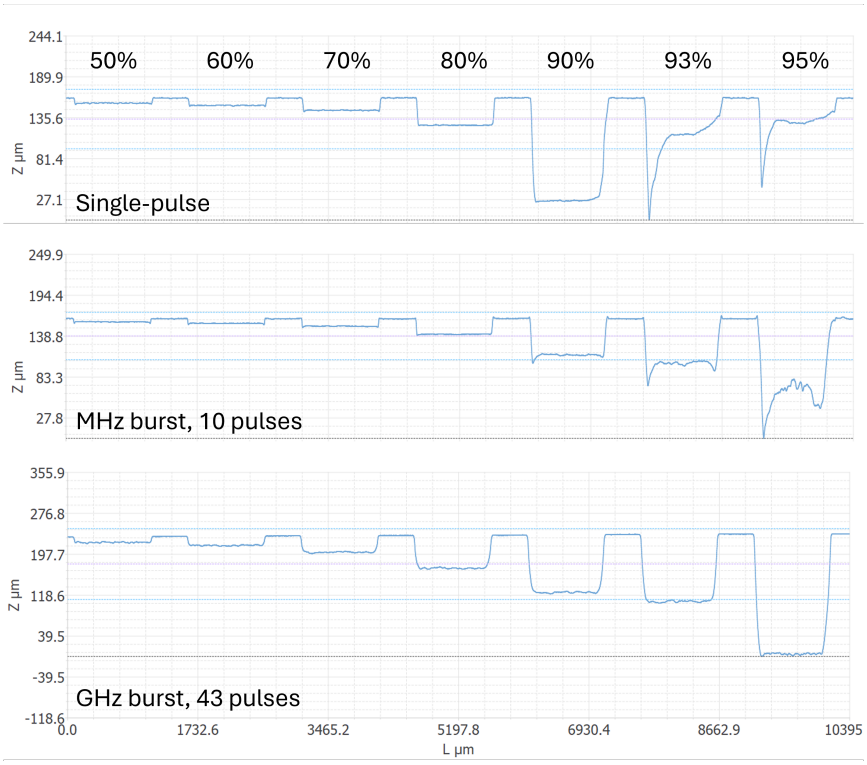

Figure 27. Image of ablated squares profile, measured with 3D optical profilometer. From left to right: 50%, 60%, 70%, 80%, 90%, 93%, and 95% pulse overlap. Noticeable reduction in ablated depth is observed at 93% and 95% pulse overlap due to material overheating. However, usage of GHz burst with 43 pulses avoids material overheating and re-deposition.

After measuring the depths of the ablated squares, the ablated volumes were calculated and divided by the "theoretical" time it took to ablate the square to determine the ablation rate (mm^3/min). From Eq. 19, we can derive that the hatching distance will be equal to:

$$x = 2\omega_0 \left(1 - \frac{PO}{100}\right). \tag{20}$$

By knowing the laser repetition rate, the required scanning speed can be calculated as:

$$v = x \cdot f. \tag{21}$$

The total number of scanned lines can be found by dividing the scanned line distance by the hatching distance and multiplying by the number of scanned layers:

$$\#lines = \frac{l}{x} \cdot n_{layers}, \tag{22}$$

where l - scanned line distance. Hence, the total time for ablating one square is calculated by dividing the total distance scanned by the scanning speed:

$$t = \frac{\#lines \cdot l}{v}. \tag{23}$$

It is important to mention that this expression of scanning time does not include scanner jump-

ing time and might differ from the actual observed time. However, this expression is sufficient for evaluating the ablation rate at different pulse overlaps. In table 2 pulse overlap, scanning speed and hatching distance are specified which were used in the experiment.

Table 2. Pulse overlap, hatching distance, and scanning speed.

Pulse Overlap (%)	**Hatching Distance (mm)**	**Scanning Speed (mm/s)**
50	0.015	3048
60	0.012	2438
70	0.009	1828
80	0.006	1219
90	0.003	609.6
93	0.0021	426.7
95	0.0015	304.8

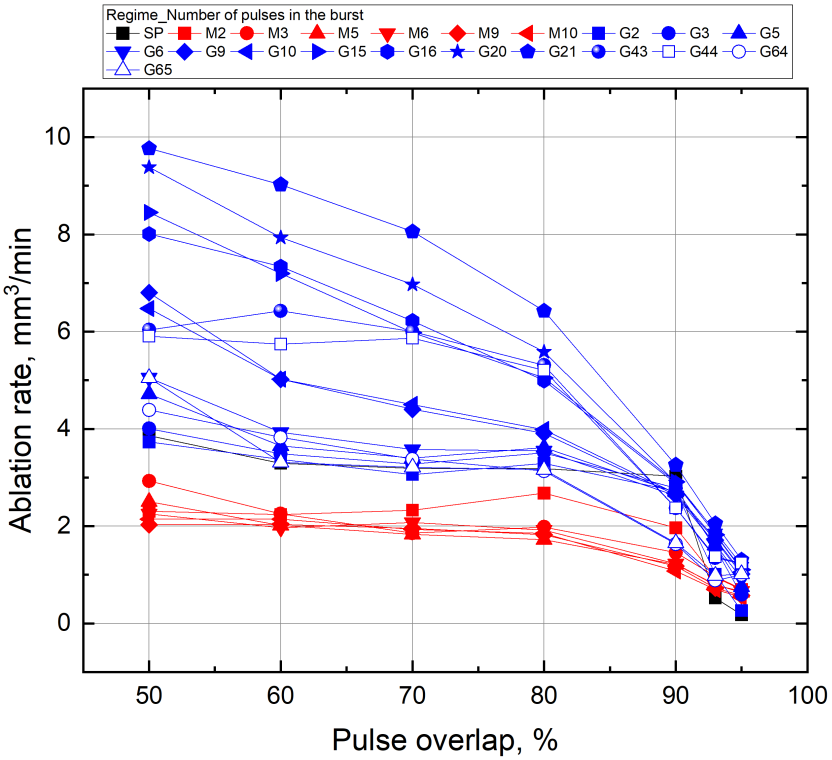

Figure 28. Ablation rate plotted against pulse overlap for various laser operation regimes. The highest ablation rate occurs at 50% pulse overlap due to the highest scanning speed and sufficient material removal measurable by the 3D optical profilometer. As the pulse overlap increases, the ablation rate decreases due to lower scanning speeds.

Having the total scanning time, the ablation rate was calculated and depicted graphically against pulse overlap in Fig. 28. The first noticeable observation is that the ablation rate is highest at 50% pulse overlap. This high ablation rate can be explained by the fact that there is still sufficient material removed at the highest speeds used in the experiment. As the pulse overlap increases, the scanning speed naturally decreases, resulting in a drop in ablation rate since the amount of material removed is too low to compensate for the decrease in scanning speed. The lower amount of material removed

with increased pulse overlap was also observed in other studies investigating Ti_6Al_4V material. The drop in ablation rate was attributed to the increased thermal load, which causes a more thermally dominated material removal process [50,51]. This trend continues from 50% to 95% pulse overlap.

As can be seen in Fig. 28 different operational regimes influence the ablation rate. The single-pulse and MHz burst regimes result in similar ablation rates throughout the pulse overlap interval. In contrast, the GHz burst regime shows a substantial increase in ablation rate, due to the increased amount of material removed from the sample. The highest ablation rate for the majority of pulse overlaps was observed for 21 pulses in the burst. When the number of pulses in the GHz burst surpasses 21, lower ablation rates are observed due to insufficient energy in the single pulse to efficiently remove the material. Therefore, at 21 pulses in the GHz burst, the most optimal ablation occurs.

From Fig. 28, it would make sense to use 50% pulse overlap, however, ablation rate is not the only dependent parameter for selecting the pulse overlap value. Another important parameter in micromachining applications is the surface roughness, which determines the quality of the process by analyzing the surface of the processed sample area. In this study, R_a was used to evaluate the surface roughness. The estimation of R_a was completed in SensoView program, which analyzed the profile of the ablated square at the middle position. SensoView program cut-out of one of the ablated square profiles can be seen in Fig. 29. The surface roughness was evaluated for all 147 squares used in ablation rate estimation when pulse overlap was changed. The results are depicted in Fig. 30, where surface roughness (R_a) is graphically visualized against pulse overlap for the different operation regimes.

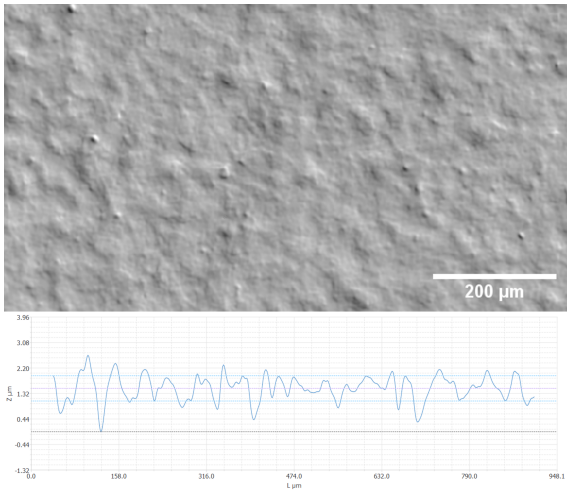

Figure 29. Image of one of the ablated square's profile in SensoView program for determining the surface roughness (R_a). Parameters: single-pulse regime, 80% pulse overlap and 1.73 J/cm^2 pulse fluence. Measured surface roughness - 0.310 µm.

From the graph in Fig. 30, it is evident that surface roughness significantly increases from 90% pulse overlap onward. With further increases in pulse overlap, in some operation regimes, it becomes impossible to measure surface roughness accurately due to material overheating which leads to substantial re-deposition of ablated material and insufficient material removal. However, it is evident that for some operation regimes, an 80% pulse overlap is optimal, resulting in the lowest surface

roughness values: single-pulse - 0.310 µm, MHz burst (10 pulses in burst) - 0.3 µm and GHz burst (5 pulses in burst) - 0.363 µm. In certain configurations, the surface roughness even falls below the initial sample surface roughness, indicated by the red dashed line. Similar findings were reported in a study by B. Fang, where the lowest surface roughness was achieved at 80% pulse overlap. At higher pulse overlaps, surface roughness increased due to increased thermal load, which degrades the surface quality [34]. However, it is important to note that from study to study, the beam diameter may vary, which can result in different optimal pulse overlap value. Interestingly, a study by G. Bonamis *et al*. noted that when long GHz bursts are used (>50 pulses per burst), thermal accumulation already occurs within the burst due to the very high intra-burst repetition rate. Consequently, the pulse overlap needs to be lower than in the single-pulse regime to avoid significant thermal defects in the process [52]. This might explain why using more than 40 pulses in the GHz burst did not result in significant changes in R_a values when the pulse overlap was varied. It is possible that the optimal pulse overlap value for long GHz bursts is less than 50%, which was not tested in this study.

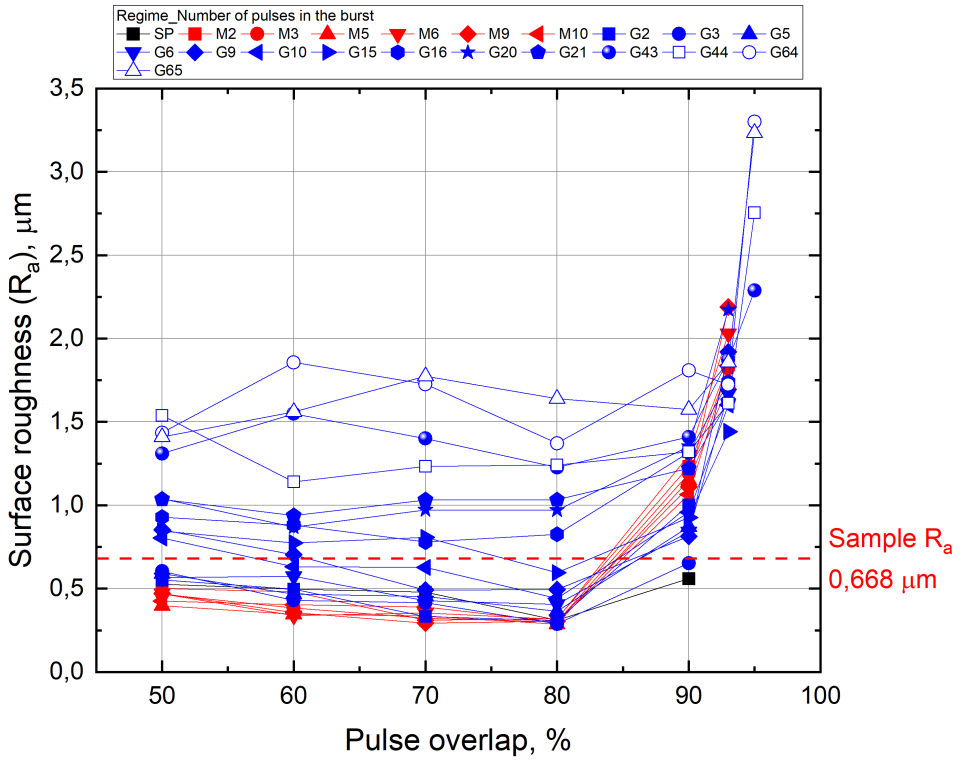

Figure 30. Surface roughness (R_a) plotted against pulse overlap at different operation regimes. As can be seen, the surface roughness tends to increase with an increase in pulse overlap. As a reference, the unprocessed sample roughness was measured, indicated by a dashed red line.

Lastly, Fig. 30 already suggests using an 80% pulse overlap. However, there may be applications where surface roughness is not as critical and ablation rate is more important. In such cases, process quality factor (Q) can be evaluated, that suggests the optimal pulse overlap based on the relative importance of ablation rate and surface roughness. For this study, the weight ratio is set at 50:50 for ablation rate and surface roughness. The process quality factor can be evaluated as the ablation

rate divided by the surface roughness value (R_a). This can also be depicted graphically, as shown in Fig. 31, which confirms the initial suggestion to use 80% pulse overlap.

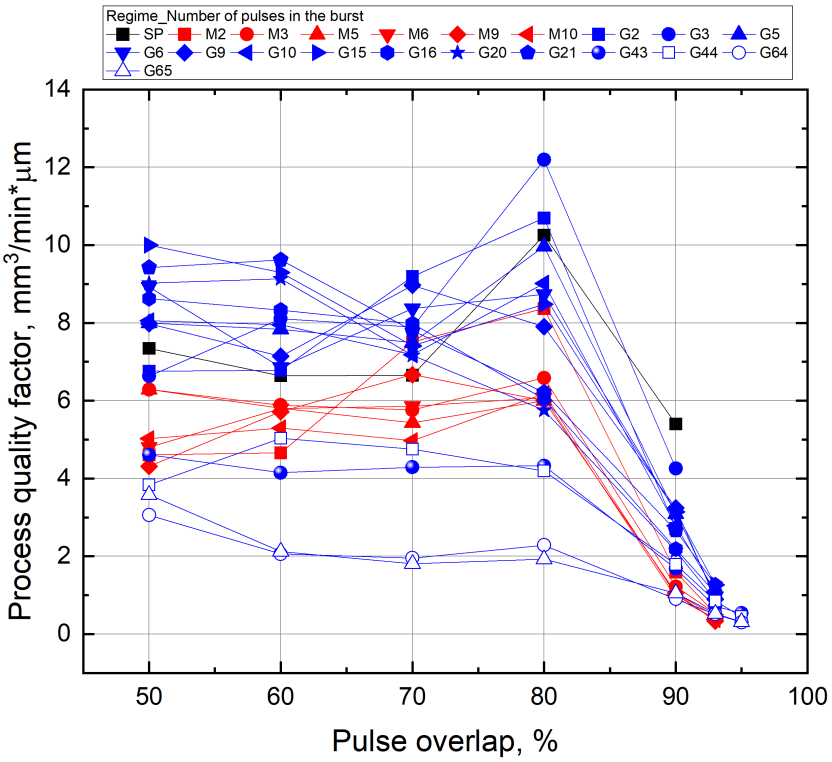

Figure 31. Process quality factor depicted graphically against pulse overlap, with a weight ratio of 50:50 for ablation rate and surface roughness. The graph indicates that 80% pulse overlap is the optimal value for processing Al_2O_3.

3.2.2 Single-Pulse, MHz Burst and GHz Burst Regime Influence to Ablation Rate

The MHz and GHz burst mode influence on ablation rate and ablation efficient was investigated by ablating squares identical to ones processed in pulse overlap investigation. 80% pulse overlap was used and the laser power was changed from 10% to 100% with steps of 10%. Various operation regimes were investigated: single-pulse, MHz burst (2, 3, 5, 6, 9, and 10 pulses in the burst) and GHz burst (2, 3, 5, 6, 9, 10, 12, 13, 15, 16, 18, 19, 21, 43, 44, 46, 47, 49, 50, 52, 53, 55, 56, 58, 59, 61, 62, 71, 72, 81, 82, 91, 92, 101, 102, 111, 112, 121, 122, 131, 132, 141, and 142 pulses in the burst). Identical to pulse overlap investigation, the processed samples were investigated with 3D optical profilometer. In total, 360 squares depths were measured. Ablation rate was calculated by dividing the removed volume by scanning time (calculated by using eq. (20-23)). The ablation rate is graphically depicted against pulse fluence in different operation regimes in Fig. 32.

Firstly, in the single-pulse regime, the ablation rate increases with pulse fluence, which aligns with expectations. The ablation rate increases from 0.90 mm^3/min to 6.39 mm^3/min with increase in pulse fluence from 1.12 J/cm^2 to 6.62 J/cm^2. Pulses with higher fluence pulses remove more material, thereby increasing the ablation rate. With sufficient spacing between pulses (80% pulse

overlap), the material does not experience overheating and re-deposition, resulting in an upward trend in ablation rate with increasing pulse fluence.

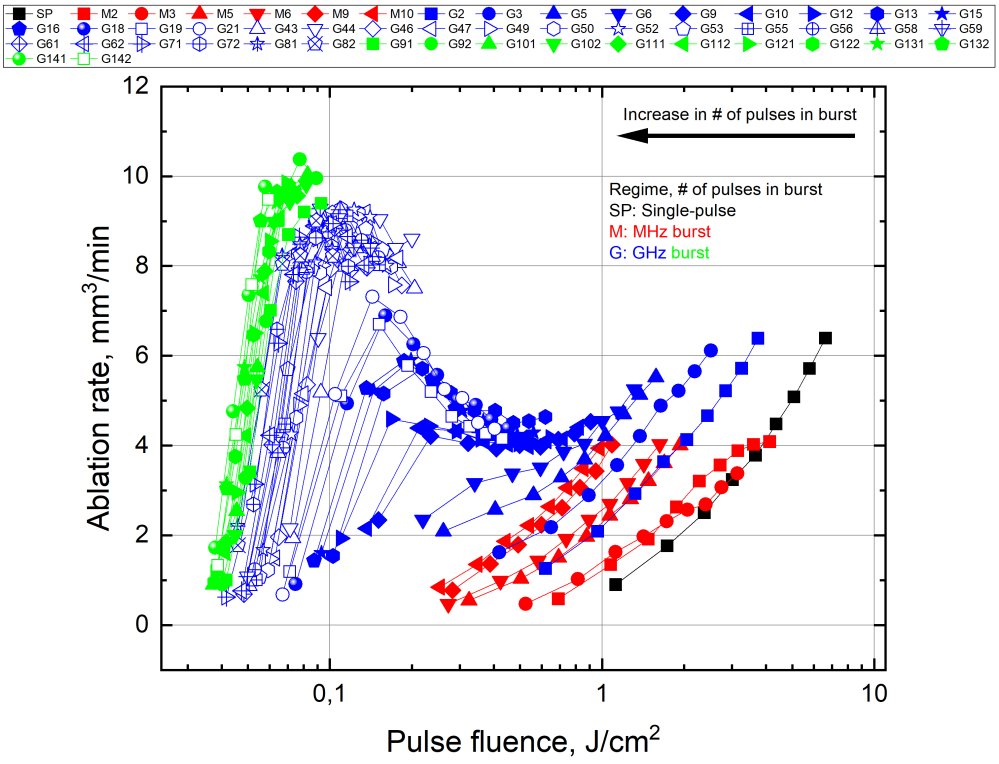

Figure 32. Ablation rate as a function of pulse fluence for various burst configurations. The graph illustrates the relationship between ablation rate and pulse fluence across single-pulse, MHz burst, and GHz burst regimes, with an increase in the number of pulses in the burst indicated from right to left.

Moving to the MHz burst regime, the ablation rate is significantly lower than in the single-pulse regime. Once the first high-energy pulse in the burst strikes the material, it creates an ablation cloud that shields subsequent pulses in the burst. This shielding decreases the ablation rate as some of the material during the shielding can be redeposited on the sample surface. Therefore, with an increase in the number of pulses in the burst, no significant change in ablation rate is observed. The reduced ablation rate in MHz burst is also observed in B. Fang *et al*., study. By increasing the number of pulses in the MHz burst from 3 to 5, the ablation rate decreased from 0.36 to 0.27 mm^3/min, which was attributed for lower energy of the pulses in the burst which does not allow efficient material ablation [34]. It is also important to note that there is no dependence on the odd/even number of pulses in the burst. This holds valid for all configurations, except for 2 and 3 pulses in the MHz burst. The reason for a slight change in ablation rate is not known because such behavior is not visible when the number of pulses in the MHz burst changes from 5 to 6. One can notice that with an increase in the number of pulses in the MHz burst (this also applies to GHz burst), the pulse fluence shifts to the left-hand side. This is expected since the single pulse fluence becomes lower with an increase in the number of pulses in the burst, as the same energy has to be divided equally among all pulses in the burst.

Lastly, moving to the GHz burst, three regimes can be observed. C. Kerse *et al*., investigated the

ablation-cooled material removal in silicon and cooper using ultrafast GHz bursts of femtosecond laser pulses. The authors explained that in the GHz burst mode, the ablation mechanism is enabled by the use of high repetition rates to prevent significant cooling between pulses. Initial pulses heat the material, and subsequent pulses ablate it before the heat can diffuse away, effectively removing thermal energy with the ablated material. This leads to high ablation efficiency and minimal thermal damage [53]. Also, G. Bonamis *et al*., investigated the ablation mechanism in GHz burst mode for silicon, copper, aluminum and stainless steel. Ablation occurs through a combination of thermal accumulation and efficient energy deposition. The firstx= pulses in the burst heat the material without causing ablation, lowering the ablation threshold for subsequent pulses. When the ablation threshold is reached, the material is efficiently ablated by the remaining pulses, achieving high ablation rates [52]. Unfortunately, up to this day, there are no scientific articles that would explain the ablation mechanism for Al_2O_3 material when it is irradiated with GHz bursts. However, keeping in mind the GHz ablation mechanisms from the publications above, we can try explaining the ablation rate dependence on pulse fluence in the GHz burst mode regime in processing Al_2O_3 material.

To begin with, when the number of pulses in the burst is below or equal to 6, there is a clear linear trend of ablation rate in increase of pulse fluence. However, by increasing the number of pulses in the GHz burst from 2 to 6, the maximum ablation rate decreases, potentially due to material heat-up from the first incident pulses and afterwards once th high energy single pulses in the burst interact with the heated material, plasma ignition occurs which shields other pulses, bringing the ablation rate down [54]. Moving on, from 9 pulses in the GHz burst, the ablation curve changes from a linear trend to a saturation curve with a peak, which becomes more recognizable with an increase in the number of pulses in the GHz burst. At the peak, the material is efficiently ablated without significant plasma formation. However, as the pulse fluence increases, plasma ignition/shielding becomes significant, reducing the ablation rate, eventually leading to saturation. G. Bonamis *et al*. also pointed out that processing in GHz burst mode with single pulse energy higher than the threshold value results in first pulses initiating ablation, avoiding the thermal accumulation step [52]. As the number of pulses in the GHz burst continues to increase, the peak ablation rate increases. This behavior continues up to 142 pulses in the GHz burst, but it is noticeable that the peak is not reached due to insufficient fluence in the single pulse in the burst. To sum up, different operation regimes exhibit the following highest ablation rates: single-pulse - 6.39 mm^3/min, MHz burst - 4.09 ^{3}/min (2 pulses in the burst), and GHz burst - 10.38 mm^3/min (92 pulses in the burst). These results show that GHz bursts can be beneficial in increasing the ablation rate by 62% in processing Al_2O_3, compared to the single-pulse regime. However, it is still not entirely clear why with increase in number of pulses in GHz burst, the maximum ablation rate increases, which requires additional studies to be done with Al_2O_3 material.

Table 3. Ablation rate and laser parameters for Al_2O_3 from various studies.

Ablation Rate (mm^3/min)	Laser Parameters	Reference
6.39	1030 nm, 350 fs, 19 W, single-pulse	this study
4.09	1030 nm, 350 fs, 23.7 W, MHz burst, 2 pulses	this study
10.38	1030 nm, 350 fs, 23.5 W, GHz burst, 92 pulses	this study
0.65	1030 nm, 400 fs, 19.8 W	[34]
0.36	1030 nm, 400 fs, 19.8 W, MHz burst, 3 pulses	[34]
0.27	1030 nm, 400 fs, 19.8 W, MHz burst, 5 pulses	[34]
129.1	1064 nm, 187 W, 10 ps	[38]
0.6	1064 nm, 2 W, <12 ps	[55]
0.02	532 nm, 3 ns, 3 W	[56]
1.2	1064 nm, 120 ns, 19.8 W	[57]

In the context of industrial applications, ablation rate is a critical parameter due to the constant need to increase process throughput. Table 3 lists ablation rates from various publications along with the laser sources used. Starting with the single-pulse regime, the acquired value of 6.39 mm^3/min surpasses other publications, likely due to the successful optimization of pulse overlap. Secondly, the MHz burst with 2 pulses results in maximum ablation rate of 4.09 mm^3/min. As previously discussed, the MHz burst results in lower ablation rates comparing to single-pulse regime, due to lower pulse energies in the burst. Also, the sufficient temporal distance between pulses allows the heat induced by the first pulse to dissipate, reducing its contribution to the ablation mechanism. Lastly, in GHz burst regime with 94 pulses, 10.38 mm^3/min ablation rate was achieved, which is the highest ablation rate value reported for Al_2O_3 processing with a femtosecond laser source with an average power of 30 W (with part of the average power lost due to many optical elements in the system). This high ablation rate is due to the effective contribution of low energy pulses, which initially heat the material and allow subsequent pulses to ablate it without inducing plasma ignition which alternatively would shield other pulses and consequently lower ablation rates. It is also important to mention that with 94 pulses in the GHz burst, the burst duration becomes $\approx$ 18 ns, which could be called pseudo-nanosecond pulse. Nonetheless, it is apparent that due to femtosecond pulses in the burst, the laser-material and ablation mechanism is different than if one would use nanosecond laser source. The ablation rate is almost 10 times higher, further confirming the benefit of GHz burst in processing Al_2O_3. It is worth mentioning that the high ablation rates observed may be due to the "theoretical" time calculation, which does not account for factors such as scanner jump time and other similar factors that can potentially increase the scanning time and affect the ablation rate.

3.2.3 Single-Pulse, MHz Burst and GHz Burst Regime Influence to Ablation Efficiency

From the calculated removed volume in different operation regimes, it is possible to evaluate the ablation efficiency, which is expressed as the ablated volume per unit power per time (mm^3/min*W). Identical to the ablation rate investigation, the ablation efficiency is graphically represented against pulse fluence in Fig. 33.

From the graph, it is visible that for single-pulse and MHz burst modes, the curve is similar

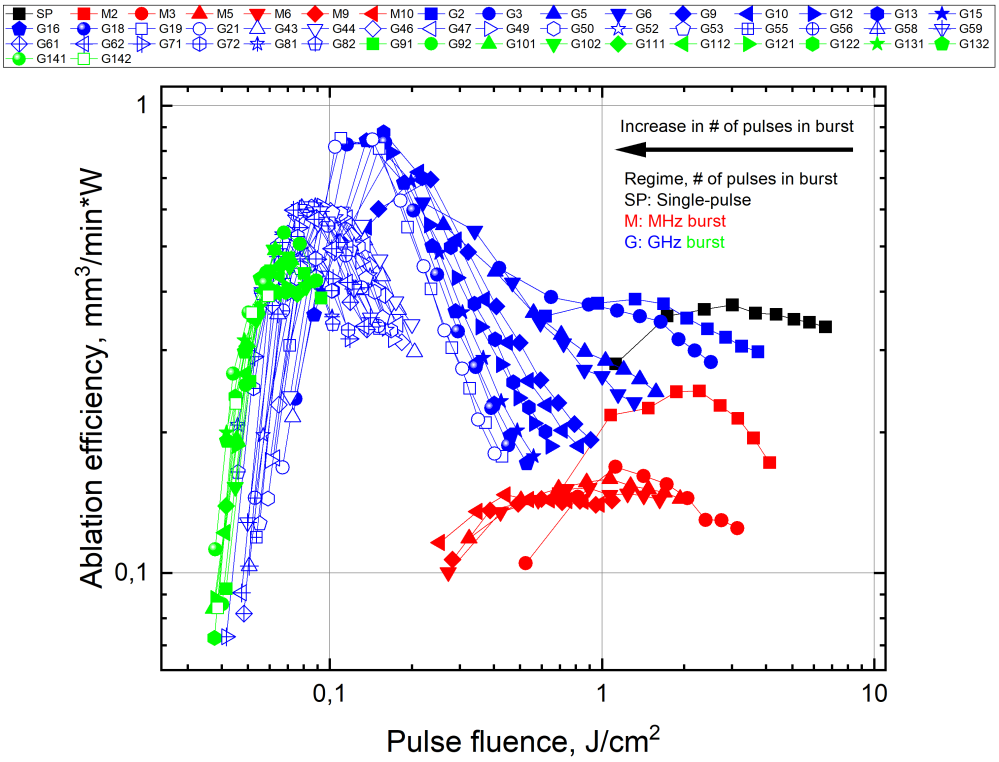

Figure 33. Ablation efficiency as a function of pulse fluence for various burst configurations. The graph illustrates the relationship between ablation efficiency and pulse fluence across single-pulse, MHz burst, and GHz burst regimes, with an increase in the number of pulses in the burst indicated from right to left.

to the theoretical one depicted in Fig. 10. With an increase in pulse fluence, the ablation efficiency increases until a maximum is reached, after which it saturates. At the peak of the curve, the ablation process is most efficient as the most material is removed per unit of induced energy or fluence. With a further increase in fluence, the amount of material removed decreases due to sufficient energy in single pulses inducing plasma ignition, which shields other pulses and re-deposits already ablated material. In the GHz burst regime, with 2 or 3 pulses in the burst, the behavior is similar to the single-pulse and MHz burst regimes. However, the initial increasing part of the ablation efficiency curve is not observed. This could be due to an insufficient number of pulses in the burst, resulting in too much fluence in the individual pulses to reach maximum ablation efficiency. When the number of pulses in the GHz burst exceeds 3, the first part of the curve becomes apparent again. The maximum ablation efficiency continues to rise with an increase in the number of pulses in the GHz burst, up to 21 pulses in the burst.

As seen in the graph, there are multiple numbers of pulses in the GHz burst that result in the most efficient ablation process. The interval starts from 12 and continues to 21 pulses in the GHz burst: G12 - 0.795 mm^3/min*W, G13 - 0.877 mm^3/min*W, G15 - 0.69 mm^3/min*W, G16 - 0.843 mm^3/min*W, G18 - 0.835 mm^3/min*W, G19 - 0.852 mm^3/min*W, and G21 - 0.847 mm^3/min*W. The highest ablation efficiency was achieved with 13 pulses in the GHz burst. As the number of pulses in the GHz burst increases, the single pulse fluence in the burst decreases, and as seen from the graph, such fluences are not high enough to ablate the material efficiently. As mentioned in

the ablation rate investigation, the high ablation efficiencies for the GHz burst are due to the high intra-burst repetition rate, which allows the first pulses in the burst to heat up the material. As the material heats up, its ϕ_{th} decreases, reaching a point where the single pulses in the burst have enough fluence to ablate the material. Since the ablation process occurs at threshold fluence values, it is very efficient, resulting in the high ablation efficiency values observed in the graph depicted in Fig. 33. Hence, the maximum ablation efficiencies for different operation regimes are as follows: single-pulse - 0.375 mm^3/min*W (pulse fluence 3.012 J/cm^2), MHz burst - 0.245 mm^3/min*W (2 pulses in the burst, pulse fluence 2.28 J/cm^2), and GHz burst - 0.877 mm^3/min*W (13 pulses in the burst, pulse fluence 0.157 J/cm^2). So, using GHz bursts, it is possible to increase ablation efficiency by 133% compared to the single-pulse regime.

3.2.4 Single-Pulse, MHz Burst and GHz Burst Regime Influence to Surface Roughness

Surface roughness was estimated for the milled squares in different operation regimes. The surface roughness was subsequently analyzed using the SensoView program, which evaluated the R_a value from the surface profile at the middle position of each ablated square for different configurations. The results are graphically depicted against pulse fluence in Fig. 34.

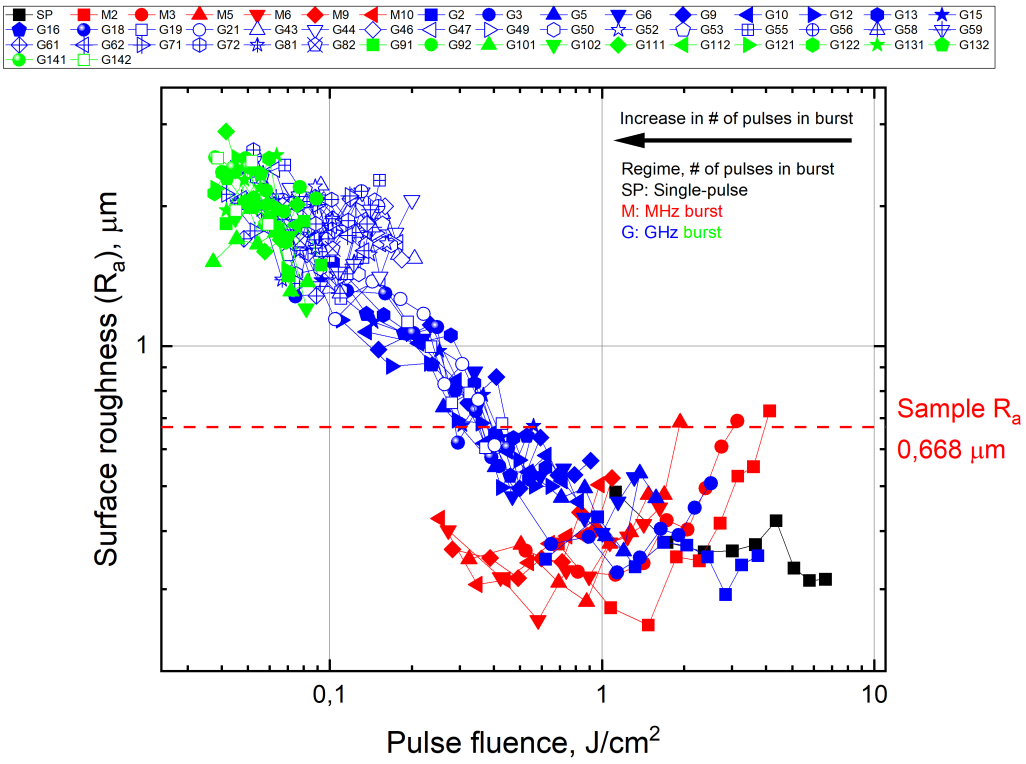

Figure 34. Surface roughness plotted against pulse fluence for various burst configurations. The graph illustrates the relationship between surface roughness and pulse fluence across single-pulse, MHz burst, and GHz burst regimes, with an increase in the number of pulses in the burst indicated from right to left.

The graph clearly shows an increase in surface roughness as the number of pulses in the burst increases. Starting with the single-pulse regime, the achieved surface roughness values are lower

than the initial sample surface roughness. Surface roughness tends to decrease with an increase in pulse fluence, which may be due to a more stable ablation process that results in a smoother surface finish. In the MHz burst regime, the values are quite scattered, but the majority of measured surface roughness values are lower than the initial sample surface roughness. At higher fluence levels, an increase in surface roughness is observed, which might be due to the re-deposition of material. In the GHz burst regime, at a low number of pulses, we observe similar behavior to the MHz burst case: the values are scattered, but the surface roughness tends to stay below the initial surface roughness. As the number of pulses increases to tens of pulses in the GHz burst, the surface roughness start to be similar to the initial sample surface roughness. The surface roughness degrades as the number of pulses in the GHz burst increases. At very high numbers of pulses in the GHz burst, the surface becomes very rough. This confirms that at longer bursts, the ablation mechanism is thermally dominated, resulting in significant increases in surface roughness due to the induced thermal effects. These findings question the ablation cooled mechanism, which as explained in literature should carry away the heat with the ablated material, until it is dissipated and cause significant thermal effects [43]. In this study, the high number of pulses in the GHz burst resulted in very rough surfaces, reaching R_a values of 2.897 µm. However, as mentioned in G. Bonamis *et al.* study, it is evident that GHz burst ablation mechanism melts and displaces material. The authors also stated that the high ablation efficiencies have also resulted in the most degraded surfaces, which is also true in this study.The most efficient ablation was observed for GHz burst with 13 pulses in the burst, at pulse fluence of 0.157 J/cm^2, which resulted in surface roughness of 1.166 µm - 1.7 times higher than the initial sample surface. Also, it is important to note that an increase in pulse fluence heavily influences the surface roughness. It is possible to decrease the R_a value from 1.166 to 0.547 µm by increasing the pulse fluence from 0.157 to 0.619 J/cm^2.

Lastly, the process quality factor was evaluated for different operation regimes by dividing the ablation rate from Fig. 32 by surface roughness from Fig. 34. The dependence of the process quality factor on pulse fluence at different operation regimes is graphically depicted in Fig. 35. To begin with, in the single-pulse regime, the process quality factor is the highest, as this regime resulted in moderate ablation rates and surface roughness. Moreover, moving to MHz and GHz burst regimes, the process quality factor drops. For the MHz burst, there is a lower amount of ablated volume due to sufficient time between pulses for the induced heat to dissipate and possible shielding. In the GHz burst, the increase in surface roughness due to the thermally dominated process at higher pulse numbers in the burst causes the process quality factor to drop even lower than in the MHz burst. From the graph, we can observe that if surface roughness is crucial for the process, the single-pulse regime is the most suitable. However, one can utilize the GHz burst to increase the ablation rate/ablation efficiency while maintaining appropriate surface roughness by performing an additional cleaning step at parameters that result in good surface roughness. For example, referring to Fig. 34, single-pulse or MHz burst (with 6 pulses in the burst) regimes are suitable for such task.

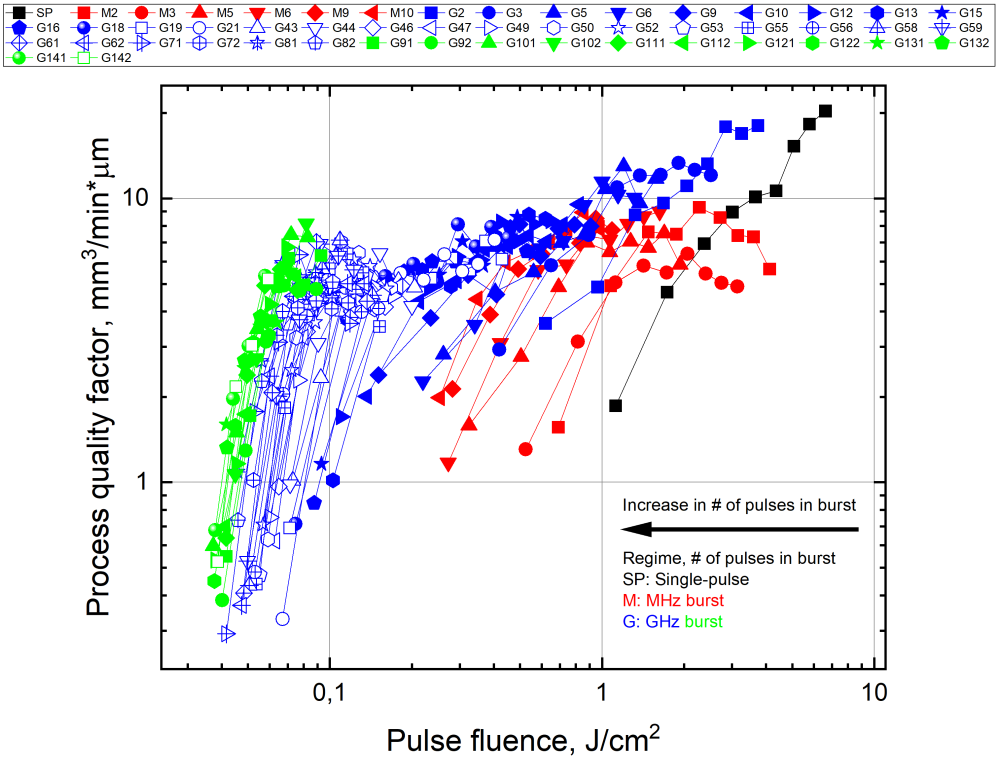

Figure 35. Process quality factor against pulse fluence for various burst configurations. The graph illustrates the relationship between process quality factor and pulse fluence across single-pulse, MHz burst, and GHz burst regimes, with an increase in the number of pulses in the burst indicated from right to left.

4. Main Findings and Conclusions

1. The D^2 method was used to measure ablation threshold fluence values for Al_2O_3 in single-pulse, MHz burst, and GHz burst regimes. The lowest ablation threshold fluence values were: single-pulse - 1.44 J/cm^2 (N=100), MHz burst - 0.38 J/cm^2 (N=100, 9 pulses), and GHz burst - 0.2 J/cm^2 (N=100, 16 pulses). The GHz burst regime achieved the lowest values due to its high intra-burst repetition rate, allowing each low fluence pulse to interact with the material efficiently.

2. The incubation factor was not evaluated since ablation threshold fluence values remained unchanged with increased N, resulting in saturation behavior. Lower N values could not be used due to the initial rough surface, making it impossible to identify the ablated crater. Also, measurements were limited to 16 pulses per burst as more pulses caused significant thermal accumulation, distorting the ablated crater form.

3. Pulse overlap investigation showed dependence on ablation rate and surface roughness. By graphing the process quality factor (composed of ablation rate and surface roughness) against different pulse overlaps, an optimal overlap of 80% was estimated.

4. Ablation rate and efficiency were investigated by milling 1x1 mm^2 squares in different operation regimes. The highest ablation rates were: single-pulse - 6.39 mm^3/min, MHz burst - 4.09 mm^3/min (2 pulses), and GHz burst - 10.38 mm^3/min (92 pulses). The highest efficiencies were: single-pulse - 0.375 mm^3/minW, MHz burst - 0.245 mm^3/minW (2 pulses), and GHz burst - 0.877 mm^3/min*W (13 pulses). The GHz burst regime had the highest ablation rates and efficiencies due to the high intra-burst repetition rate. First pulses in the burst heat the material, lowering its ablation threshold. When the ablation threshold is reduced to single pulse fluence, the ablation occurs with high efficiency.

5. The burst mode's influence on surface roughness was investigated by evaluating the R_a value. Surface roughness increased with more pulses in the burst for both MHz and GHz regimes. In the GHz regime with >43 pulses, the surface became very rough, confirming a thermally dominated ablation mechanism. However, increasing pulse fluence decreased the R_a from 1.166 to 0.547 µm by increasing the pulse fluence from 0.157 to 0.619 J/cm^2.

6. Process quality factor analysis against pulse fluence indicated that the single-pulse regime is optimal when both ablation rate and surface roughness matter equally. If ablation rate is prioritized, the GHz burst regime is the most suited operation regime, however in this regime surface roughness increases. The surface finish can be improved afterwards with a second scan using parameters that result in low roughness, such as single-pulse or MHz burst with 6 pulses.

References

[1] S. Rung, N. Häcker, and R. Hellmann, Micromachining of alumina using a high-power ultrashort-pulsed laser, *Materials*, Aug 2022, **15**.

[2] W. Perrie, A. Rushton, M. Gill, P. Fox, and W. O'Neill, Femtosecond laser micro-structuring of alumina ceramic, *Applied Surface Science*, 2005, **248**, 213–217.

[3] X. C. Wang, H. Y. Zheng, P. L. Chu, *et al.*, Femtosecond laser drilling of alumina ceramic substrates, *Applied Physics A: Materials Science and Processing*, 11 2010, **101**, 271–278.

[4] P. Auerkari, *Mechanical and Physical Properties of Engineering Alumina Ceramics*. No. 1792 in VTT Tiedotteita - Meddelanden - Research Notes, Finland: VTT Technical Research Centre of Finland, 1996.

[5] C. Liang, Z. Li, C. Wang, K. Li, Y. Xiang, and X. Jia, Laser drilling of alumina ceramic substrates: A review, *Optics and Laser Technology*, Dec 2023, **167**.

[6] R. N. Oosterbeek, T. Ward, S. Ashforth, O. Bodley, A. E. Rodda, and M. C. Simpson, Fast femtosecond laser ablation for efficient cutting of sintered alumina substrates, *Optics and Lasers in Engineering*, 2016, **84**, 105–110.

[7] S. H. Kim, I. B. Sohn, and S. Jeong, Ablation characteristics of aluminum oxide and nitride ceramics during femtosecond laser micromachining, *Applied Surface Science*, Sep 2009, **255**, 9717–9720.

[8] Y. Zhang, Y. Ito, H. Sun, and N. Sugita, Investigation of multi-timescale processing phenomena in femtosecond laser drilling of zirconia ceramics, *Optics Express*, Oct 2022, **30**, 37394.

[9] T. H. Maiman, Stimulated optical radiation in ruby, *Nature*, Aug 1960, **187**, 493–494.

[10] B. N. Chichkov, C. Momma, S. Nolte, F. Y. Alvensleben, and A. Tiinnermann, Femtosecond, picosecond and nanosecond laser ablation of solids, *Applied Physics A: Materials Science and Processing*, 1996, **63**, 109–115.

[11] C. Min, X. Yang, M. Xue, Q. Li, W. Wang, and X. Mei, Micromachining porous alumina ceramic for high quality trimming of turbine blade cores via double femtosecond laser scanning, *Ceramics International*, Jan 2021, **47**, 461–469.

[12] T. P. Callou, R. Garcia, A. Mukai, N. T. Giacomin, R. G. de Souza, and S. J. Bechara, Advances in femtosecond laser technology, *Clinical Ophthalmology*, Apr 2016, **10**, 697–703.

[13] K. Sugioka and Y. Cheng, Femtosecond laser three-dimensional micro-and nanofabrication, *Applied Physics Reviews*, Dec 2014, **1**.

[14] A. Žemaitis, M. Gaidys, M. Brikas, P. Gečys, G. Račiukaitis, and M. Gedvilas, Advanced laser scanning for highly-efficient ablation and ultrafast surface structuring: experiment and model, *Scientific Reports*, Dec 2018, **8**.

[15] A. Žemaitis, Efficient laser ablation for bio-inspired 3d functional surfaces, 2022.

[16] A. Butkutė and L. Jonušauskas, 3D Manufacturing of Glass Microstructures Using Femtosecond Laser, *Micromachines*, 2021, **12**.

[17] R. R. Birge and B. M. Pierce, Semiclassical time-dependent theory of two-photon spectroscopy. the effect of dephasing in the virtual level on the two-photon excitation spectrum of isotachysterol, *International Journal of Quantum Chemistry*, 1986, **29**, 639–656.

[18] P. Balling and J. Schou, Femtosecond-laser ablation dynamics of dielectrics: Basics and applications for thin films, *Reports on Progress in Physics*, Mar 2013, **76**.

[19] S. S. Mao, F. Quéré, S. Guizard, X. Mao, R. E. Russo, G. Petite, and P. Martin, Dynamics of femtosecond laser interactions with dielectrics, *Applied Physics A: Materials Science and Processing*, Nov 2004, **79**, 1695–1709.

[20] N. Bulgakova, A. Bulgakov, V. Zhukov, W. Marine, A. Vorobyev, and C. D, Charging and plasma effects under ultrashort pulsed laser ablation, *Proc SPIE*, May 2008, **7005**, 70050C.

[21] R. Lausten and P. Balling, On-the-fly depth-profiling during ablation with ultrashort laser pulses: A tool for accurate micromachining and laser surgery, *Applied Physics Letters*, 2001, **79**, 884–886.

[22] P. J. L. Webster, J. X. Z. Yu, B. Y. C. Leung, M. D. Anderson, V. X. D. Yang, and J. M. Fraser, In situ 24 khz coherent imaging of morphology change in laser percussion drilling, *Opt. Lett.*, Mar 2010, **35**, 646–648.

[23] J. M. Liu, Simple technique for measurements of pulsed gaussian-beam spot sizes, *Opt. Lett.*, May 1982, **7**, 196–198.

[24] J. Bonse, J. M. Wrobel, J. Krüger, and W. Kautek, Ultrashort-pulse laser ablation of indium phosphide in air, *Applied Physics A: Materials Science and Processing*, 2001, **72**, 89–94.

[25] Y. Jee, M. Becker, and R. Walser, Laser-induced damage on single-crystal metal surfaces, *Journal of The Optical Society of America B-optical Physics - J OPT SOC AM B-OPT PHYSICS*, Mar 1988, **5**.

[26] S. Wellershoff, J. Hohlfeld, J. Güdde, and E. Matthias, The role of electron-phonon coupling in femtosecond laser damage of metals, *Applied Physics A*, Dec 1999, **69**, S99–S107.

[27] J. Bonse, P. Rudolph, J. Krüger, S. Baudach, and W. Kautek, Femtosecond pulse laser processing of tin on silicon, *Applied Surface Science*, 2000, **154-155**, 659–663.

[28] S. Baudach, J. Bonse, J. Krüger, and W. Kautek, Ultrashort pulse laser ablation of polycarbonate and polymethylmethacrylate, *Applied Surface Science*, 2000, **154-155**, 555–560.

[29] A. Rosenfeld, M. A. Lorenz, R. Stoian, and D. Ashkenasi, Ultrashort-laser-pulse damage threshold of transparent materials and the role of incubation, *Applied Physics A*, 1999, **69**, S373–S376.

[30] A. Hertwig, S. Martin, J. Krüger, and W. Kautek, Surface damage and color centers generated by femtosecond pulses in borosilicate glass and silica, *Applied Physics A*, Sep 2004, **79**, 1075–1077.

[31] L. Omenaca, M. Gomez-Aranzadi, I. Ayerdi, and E. Castano, Numerical simulation and experimental validation of ultrafast laser ablation on aluminum, *Optics and Laser Technology*, 2024, **170**, 110283.

[32] R. Samad and N. Vieira, Geometrical method for determining the surface damage threshold for femtosecond laser pulses, *Laser Phys.*, Feb 2006, **16**, 336–339.

[33] J. Weixler, M. Zweifel, and K. Wegener, 300 fs pulsed laser ablation of Al_2O_3 ceramic and introduction of a predictive model, *Materials and Design*, May 2022, **217**.

[34] B. Fang, C. Ma, and X. Wang, A composite strategy for high-quality and high-efficiency milling of alumina ceramic via femtosecond laser burst-mode, *International Journal of Advanced Manufacturing Technology*, Apr 2023, **125**, 3191–3204.

[35] N. Ackerl and K. Wegener, Ablation characteristics of alumina and zirconia ceramics on ultrashort pulsed laser machining, *Journal of Laser Micro Nanoengineering*, 2019, **14**, 168–172.

[36] G. Račiukaitis, M. Brikas, P. Gečys, B. Voisiat, and M. Gedvilas, Use of high repetition rate and high power lasers in microfabrication: How to keep the efficiency high?, *Journal of Laser Micro Nanoengineering*, 2009, **4**, 186–191.

[37] M. Gaidys, A. Žemaitis, P. Gečys, and M. Gedvilas, Efficient picosecond laser ablation of copper cylinders, *Applied Surface Science*, Jul 2019, **483**, 962–966.

[38] J. Schille, L. Schneider, A. Streek, S. Kloetzer, and U. Loeschner, High-throughput machining using a high-average power ultrashort pulse laser and high-speed polygon scanner, *Optical Engineering*, 2016, **55**, 096109.

[39] A. Žemaitis, M. Gaidys, P. Gečys, G. Račiukaitis, and M. Gedvilas, Rapid high-quality 3d micro-machining by optimised efficient ultrashort laser ablation, *Optics and Lasers in Engineering*, Mar 2019, **114**, 83–89.

[40] A. Žemaitis, M. Gaidys, P. Gečys, M. Barkauskas, and M. Gedvilas, Femtosecond laser ablation by bibursts in the MHz and GHz pulse repetition rates, *Opt. Express*, Mar 2021, **29**, 7641–7653.

[41] J. Mur and R. Petkovšek, Near-THz bursts of pulses – Governing surface ablation mechanisms for laser material processing, *Applied Surface Science*, 2019, **478**, 355–360.

[42] R. Mayerhofer, Ultrashort-pulsed laser material processing with high repetition rate burst pulses, in *Laser Applications in Microelectronic and Optoelectronic Manufacturing (LAMOM) XXII*, vol. 10091, 100910Z, International Society for Optics and Photonics, SPIE, 2017.

[43] X. Wolters, G. Bonamis, K. Mishchick, E. Audouard, C. Hönninger, and E. Mottay, High power GHz femtosecond laser for ablation efficiency increase, *Procedia Manufacturing*, 2019, **36**, 200–207.

[44] R. D. Palo, A. Volpe, C. Gaudiuso, P. Patimisco, V. Spagnolo, and A. Ancona, Threshold fluence and incubation during multi-pulse ultrafast laser ablation of quartz, *Opt. Express*, Dec 2022, **30**, 44908–44917.

[45] H. Sakurai, Y. Iida, A. Mizutani, K. Konishi, J. Yumoto, and M. Kuwata-Gonokami, Wavelength Dependence of the Laser-Induced Damage Threshold of α-Al_2O_3, in *Conference on Lasers and Electro-Optics*, 1–2, Optica Publishing Group, 2016.

[46] H. Mustafa, M. Mezera, D. Matthews, and G.-W. Römer, Effect of surface roughness on the ultrashort pulsed laser ablation fluence threshold of zinc and steel, *Applied Surface Science*, 05 2019, **488**.

[47] M. Sun, J. Zhu, and Z. Lin, Modeling of ablation threshold dependence on pulse duration for dielectrics with ultrashort pulsed laser, *Optical Engineering*, Nov 2016, **56**, 011026.

[48] G. Mincuzzi, E. Audouard, A. Bourtereau, *et al.*, Pulse to pulse control for highly precise and efficient micromachining with femtosecond lasers, *Opt. Express*, Jun 2020, **28**, 17209–17218.

[49] C. Li, M. A. Argument, Y. Y. Tsui, and R. Fedosejevs, Micromachining with femtosecond 250-nm laser pulses, in *Applications of Photonic Technology 4* (R. A. Lessard and G. A. Lampropoulos, eds.), vol. 4087, 1194 – 1200, International Society for Optics and Photonics, SPIE, 2000.

[50] F. Yang, R. Kang, H. Ma, G. Ma, D. Wu, and Z. Dong, Effect of femtosecond laser processing parameters on the ablation microgrooves of rb-sic composites, *Materials*, 2023, **16**.

[51] G. Schnell, U. Duenow, and H. Seitz, Effect of laser pulse overlap and scanning line overlap on femtosecond laser-structured ti6al4v surfaces, *Materials*, 2020, **13**.

[52] G. Bonamis, E. Audouard, C. Hönninger, J. Lopez, K. Mishchik, E. Mottay, and I. Manek-Hönninger, Systematic study of laser ablation with GHz bursts of femtosecond pulses, *Opt. Express*, Sep 2020, **28**, 27702–27714.

[53] C. Kerse, H. Kalaycioglu, P. Elahi, *et al.*, Ablation-cooled material removal with ultrafast bursts of pulses, *Nature*, Jul 2016, **537**.

[54] K. Obata, F. Caballero-Lucas, and K. Sugioka, Material processing at GHz burst mode by femtosecond laser ablation, *Journal of Laser Micro Nanoengineering*, 2021, **16**, 19–23.

[55] D. Karnakis, G. Rutterford, M. Knowles, T. Dobrev, P. Petkov, and S. Dimov, High quality laser milling of ceramics, dielectrics and metals using nanosecond and picosecond lasers, in *Photon Processing in Microelectronics and Photonics V*, vol. 6106, 610604, International Society for Optics and Photonics, SPIE, 2006.

[56] J. Han, K. K. Saxena, A. Braem, D. Reynaerts, and S. Castagne, Influence of material composition on nanosecond pulsed laser micromachining of zirconia-alumina composites, in *Procedia CIRP*, vol. 113, 605–610, Elsevier, 2022.

[57] E. Williams, E. Brousseau, and A. Rees, Nanosecond Yb fibre laser milling of aluminium: effect of process parameters on the achievable surface finish and machining efficiency, *International Journal of Advanced Manufacturing Technology*, Sep 2014, **74**, 769–780.

Abliacijos Efektyvumo Tyrimas Aliuminio Oksido Keramikoje Naudojant Femtosekundinį Lazerį MHz/GHz Papliūpų Režime

Deividas Andriukaitis

Santrauka

Keramika yra populiari medžiaga, kuri yra taikoma daugelyje sričių: medicinoje, automobilių pramonėje, elektronikos industrijoje ir kitose. Keramikos apdirbimui dažniausiai naudojami mechaniniai procesai, tokie kaip frezavimas, gręžimas ir pjovimas. Deja, mechaninis apdirbimas turi keletą trūkumų: įrankių dylimas, brangūs įrankiai reikalingi medžiagos apdirbimui, ir ribotas apdirbimo tikslumas. Lazerinis apdirbimas jau kurį laiką yra integruojamas į industrinius procesus dėl galimybės apdirbti įvairiausias medžiagas, įskaitant ir keramiką, tuo pat metu išvengiant mechaninio apdirbimo trūkumų.

Femtosekundinis lazerinis apdirbimas yra tinkama technologija kietoms ir trapioms medžiagoms, tokioms kaip aliuminio oksido keramika, apdirbti, užtikrinant aukštą apdirbimo kokybę. Tačiau femtosekundinių lazerių apdirbimo sparta vis dar atsilieka nuo kitų metodų, o tai trukdo technologijai pilnai integruotis į industrinius taikymus. Vienas būdų padidinti spartą yra naudoti papliūpų režimą, kuriame femtosekundinis lazeris iššauna impulsų traukinius MHz arba GHz dažniu.

Šio darbo tikslas buvo įvertinti MHz/GHz papliūpų režimų įtaką aliuminio oksido keramikos abliacijos efektyvumui ir spartai. Tyrimas buvo atliktas keičiant lazerio galią, impulsų persiklojimo procentą ir papliūpų režimus. Rezultatai parodė, kad GHz papliūpos yra tinkamiausios aliuminio oksido apdirbimui. Dėl didelio pasikartojimo dažnio pirmieji mažos energijos impulsai papliūpoje medžiagą kaitina ir mažina jos pažeidimo slenkstį. Kuomet pažeidimo slenkstis sumažėja iki pavienio impulso papliūpoje energijos, įvyksta efektyvi medžiagos abliacija. Taigi, naudojant GHz papliūpas, abliacijos sparta buvo padidinta nuo 6,39 mm^3/min iki 10,38 mm^3/min, o abliacijos efektyvumas – nuo 0,375 mm^3/min*W iki 0,877 mm^3/min*W.